

A Star Formation Law for Dwarf Irregular Galaxies

Bruce G. Elmegreen

*IBM Research Division, T.J. Watson Research Center, 1101 Kitchawan Road, Yorktown Heights,
NY 10598, bge@us.ibm.com*

Deidre A. Hunter

Lowell Observatory, 1400 West Mars Hill Road, Flagstaff, Arizona 86001, dah@lowell.edu

ABSTRACT

The radial profiles of gas, stars, and far ultraviolet radiation in 20 dwarf Irregular galaxies are converted to stability parameters and scale heights for a test of the importance of two-dimensional (2D) instabilities in promoting star formation. A detailed model of this instability involving gaseous and stellar fluids with self-consistent thicknesses and energy dissipation on a perturbation crossing time give the unstable growth rates. We find that all locations are effectively stable to 2D perturbations, mostly because the disks are thick. We then consider the average volume densities in the midplanes, evaluated from the observed HI surface densities and calculated scale heights. The radial profiles of the star formation rates are equal to about 1% of the HI surface densities divided by the free fall times at the average midplane densities. This 1% resembles the efficiency per unit free fall time commonly found in other cases. There is a further variation of this efficiency with radius in all of our galaxies, following the exponential disk with a scale length equal to about twice the stellar mass scale length. This additional variation is modeled by the molecular fraction in a diffuse medium using radiative transfer solutions for galaxies with the observed dimensions and properties of our sample. We conclude that star formation is activated by a combination of three-dimensional gaseous gravitational processes and molecule formation. Implications for outer disk structure and formation are discussed.

Subject headings: ISM: kinematics and dynamics — ISM: molecules — Galaxies: dwarf
— Galaxies: star formation

1. Introduction

The outer parts of spiral galaxies (Kennicutt 1989) and most of dwarf irregular galaxies (Hunter & Plummer 1996; Meurer et al. 1996; van Zee et al. 1997; Hunter et al. 1998) appear to be marginally or wholly stable according to the common Toomre condition for a single fluid disk of zero thickness. However, star formation still occurs there (Ferguson et al. 1998; LeLièvre & Roy 2000; Thilker et

al. 2005; Gil de Paz et al. 2005; Hunter et al. 2011), suggesting either that the outer disks are unstable anyway, or that some other triggering mechanism is operating to form stars. The most inclusive stability models consider both stars and gas in a thick disk (Romeo 1992; Rafikov 2001; Elmegreen 2011). Leroy et al. (2008) showed that with the Rafikov 2-fluid stability criterion, the main parts of spiral and irregular galaxies are marginally unstable. Yang et al. (2007) showed the same thing for the main part of the LMC. The far-outer parts of galaxies and dwarfs are still a problem, though: the gas mass surface density usually dominates the stellar mass surface density, and both get exponentially low with increasing radius, driving up the stability parameter Q (e.g., Yim et al. 2014).

Another difference between the inner and outer parts of galaxies is the slope of the relationship between the star formation rate (SFR) per unit area and the gas surface density. In the inner parts of disks, this slope varies between unity for the molecular gas (Wong & Blitz 2002; Leroy et al. 2008; Bigiel et al. 2008) and 1.5 or so for the total gas (Kennicutt et al. 2007; see reviews in Kennicutt & Evans 2012 and Dobbs et al. 2013). In the outer parts it can be much steeper, more like 2 to 3 (Bigiel et al. 2008, 2010). The linear relationship in the inner part is somewhat sensible, showing that more gas makes more stars with a nearly constant consumption time at the characteristic density of CO emission (Krumholz et al. 2009a; Lada et al. 2013). The linear law also gives a reasonable SFR over cosmic time (Feldmann 2013). There are assumptions in deriving this law, however, such as the background subtraction for diffuse CO (Shetty et al. 2013, 2014) and star formation tracers (Liu et al. 2011; Rahman et al. 2011), the level of variations in the CO excitation (Momose et al. 2013), and possible variations in the conversion from CO to H₂ (Boissier et al. 2003). The quadratic slope in the outer part may contain the same dependence on molecules as the inner part, although molecules are a trace component in the outer part (Schruba et al. 2011), but also involve variations in the molecular fraction and thermal phase of the gas (Ostriker et al. 2010; Krumholz 2013).

The outer parts are also where the disk gets thick, presumably because of the exponential drop in surface density Σ combined with a slower decrease in the vertical velocity dispersion σ (Dib et al. 2006; van der Kruit & Freeman 2011). Such a flare follows from the equation for scale height in an isothermal gas, $H = \sigma^2 / (\pi G \Sigma)$. The disk flare means that the midplane density drops doubly fast, because it equals the ratio of Σ to $2H$. If the fundamental star formation law is three-dimensional (3D; e.g., Ferguson et al. 1998; Elmegreen 2002; Krumholz et al. 2012), and not two-dimensional (2D) like the spiral wave instability originally targeted for the Q parameter (Toomre 1964), then the change from a linear to a quadratic star formation law with radius could result in part from the flare (e.g., Barnes et al. 2012).

Here we consider the applicability of the 2D, thick-disk gravitational instability model to 20 dwarf irregular (dIrr) galaxies that have most of their star formation in the quadratic regime (Bigiel et al. 2008) and are among the class of galaxies that have relatively thick disks (Hodge & Hitchcock 1966; van den Bergh 1988; Staveley-Smith et al. 1992). Equilibrium models of the disk thicknesses in four dwarf galaxies, based on HI and other data in the THINGS survey, were also in Banerjee

et al. (2011). Our analysis of thickness is similar to theirs, based on the multi-component model of vertical equilibrium in Narayan & Jog (2002).

We find that, considering disk thickness, nearly all of our dIrrs are effectively stable in two dimensions throughout. That is, their instability growth times are all very long, as calculated for a gas+star mixture with equilibrium disk thicknesses and gaseous energy dissipation on a perturbation crossing time, as in a realistic turbulent medium (Elmegreen 2011). This appears to rule out 2D instabilities as a model for star formation. We then investigate the possible role of 3D processes by considering the dynamical time at the midplane density, rather than the growth time of a 2D instability. We consider that the SFR per unit area scales with the product of the HI gas column density and the dynamical rate from the 3D density (as in, e.g., Elmegreen 2002; Krumholz et al. 2009a, 2012). The multiplicative factor that connects these two rates turns out to be the usual $\sim 1\%$ (Krumholz & Tan 2007). Thus, star formation still follows 3D gravitational processes even where the conventional Toomre Q parameter predicts a high level of 2D stability.

We also find a residual dependence of this multiplicative factor on radius, for which two models are considered. The first model has the SFR connected to the HI dynamical rate by an efficiency factor ϵ_{ff} that is proportional to the molecular fraction when both the molecular and atomic layers have the same radial dependence for thickness. In this model, the radiation field that determines the molecular fraction has a volume emissivity proportional to the stellar density. The second model has the SFR connected directly to the H_2 dynamical rate with a constant efficiency and assumes the thickness of the molecular layer is constant with radius. For this, the radiation field that determines the molecular fraction has a volume emissivity proportional to the density of FUV radiation. In both cases, the molecular fraction is determined from radiative transfer solutions in a diffuse medium using the observed or derived average gradients in stellar density and intensity, gas density, and scale height.

Additional models consider the variation of the molecular fraction with radius using the formalism in Krumholz et al. (2009a,b) and using another method that integrates over the probability distribution function for cloud column density with a separation between high column clouds that form molecules and low column clouds that do not. In both cases, the usual threshold behavior for the formation of H_2 appears, suggesting a sudden drop in molecular fraction at some radius in the galaxy. Such a drop is not observed in the star formation rates here and may not be appropriate for the far-outer regions of galaxies which presumably have a low molecular fraction throughout.

In what follows, Section 2 describes the observations, Section 3 demonstrates that the dIrrs in our survey have relatively thick disks, Section 4 shows they are significantly stabilized by thickness against 2D disk instabilities, and Section 5 considers a fundamental star formation law based on 3D dynamical processes with some efficiency. Section 6.1 looks at the radial trends in our data for the purpose of understanding a radial trend found in the efficiency. Section 6.2 considers that this efficiency trend results from variations in the molecular fraction in a diffuse interstellar medium, which depends on molecular self-shielding and mutual shielding inside of and between diffuse clouds.

The molecular fraction depends on the radiation field, so we solve the equation of radiative transfer for a dIrr galaxy in Section 6.3 using the average radial trends for gaseous and stellar densities and scale heights. A model using FUV radiation for molecular dissociation (Section 6.4) requires a uniform line-of-sight thickness for the H₂ clouds, rather than a disk flare as inferred for the HI. Other models considering a threshold behavior for H₂ formation are in Section 6.5. A discussion about the implications of these results for the outer edges of galaxies is in Section 7. The conclusions are in Section 8.

2. Observations

The 20 dIrr galaxies used in this study are a sub-sample of the 41 galaxies that constitute the LITTLE THINGS (Local Irregulars That Trace Luminosity Extremes, The HI Nearby Galaxy Survey) sample (Hunter et al. 2012). The galaxies listed in Table 1 were chosen from the larger sample to be those having stellar mass density profiles in Zhang et al. (2012) and HI rotation curves in Oh et al. (2015). The galaxies are relatively nearby (<10.3 Mpc), gas-rich, and have recent star formation. One galaxy, the Blue Compact Dwarf Haro 29, is suspected of having undergone a recent interaction (Ashley et al. 2013). Otherwise, the sample galaxies are expected to be representative of dIrrs with on-going star formation through primarily internal processes.

The gas data used here were derived from cubes of HI emission as a function of velocity obtained with the Very Large Array (VLA¹). The observations, calibration and mapping procedures are described by Hunter et al. (2012). The rotation curves were determined using a tilted-ring model through an iterative process that deconvolves bulk rotation from non-circular motions (Oh et al. 2011, 2014). Here, we use the observed rotation curves before an asymmetric drift correction is applied because that is appropriate for the actual gas angular momentum and the value of κ in the Toomre parameter Q . The HI mass density profiles were determined from the Naturally-weighted integrated HI (moment zero) maps using the parameters determined from the rotation curve fitting (center, position angle, inclination, annuli width). The HI mass was multiplied by 1.36 to include He. Uncertainties in the azimuthally averaged gas mass are estimated to be < 10%. The gas velocity dispersion profiles were measured from the flux-weighted dispersion (moment 2) maps also derived from the Naturally-weighted HI cubes.

The stellar mass surface density profiles are from Zhang et al. (2012). That study performed spectral energy distribution (SED) fitting to surface photometry from *Galaxy Evolution Explorer* (GALEX, Martin et al. 2005) FUV and NUV, Lowell Observatory *UBV* and H α , and *Spitzer* (Werner et al. 2004) 3.6 μ m images (Fazio et al. 2004). The stellar azimuthally-averaged surface photometry used ellipse parameters appropriate to the stellar disk and determined from the *V*-band

¹ The VLA is a facility of the National Radio Astronomy Observatory (NRAO). The NRAO is a facility of the National Science Foundation operated under cooperative agreement by Associated Universities, Inc. These data were taken during the upgrade of the VLA to the Expanded VLA, now JVLA.

image (Hunter & Elmegreen 2006). Modeling the photometry used a library of 4×10^6 star formation histories and lifetimes divided into six logarithmic age bins. A Chabrier IMF was assumed.

The stellar velocity dispersions are evaluated from the expression $\sigma_{\text{star}} = 10.0^{-0.15M_B - 1.27} \text{ km s}^{-1}$ (Swaters 1999; Johnson et al. 2012, 2015) for B-band absolute magnitude M_B . These dispersion are assumed to be constant with radius.

The current SFRs are taken as proportional to the FUV surface photometry, given in Hunter et al. (2010) and updated by Zhang et al. (2012) to use a more recent data reduction pipeline and to include all of the LITTLE THINGS galaxies. The surface brightnesses, μ_{FUV} , used here are AB magnitudes per square arcsec corrected for extinction. The FUV surface photometry is converted to a SFR surface density based on a multiplicative factor between L_{FUV} and SFR_{FUV} given by Kennicutt (1998) and modified for the sub-solar metallicities of the dIrrs by Hunter et al. (2010). The result is $\Sigma_{\text{SFR}} = 10^{-0.4\mu_{\text{FUV}} + 7.415} M_{\odot} \text{ pc}^{-2} \text{ Myr}^{-1}$ for a Salpeter IMF. For a Chabrier IMF, the mass is smaller by the factor 0.55, and that is what we use here: $\Sigma_{\text{SFR}} = 10^{-0.4\mu_{\text{FUV}} + 7.155} M_{\odot} \text{ pc}^{-2} \text{ Myr}^{-1}$. The FUV flux density is obtained by the usual formula, $F_{\text{FUV}} = 10^{-0.4(\mu_{\text{FUV}} + 48.6)} \text{ erg cm}^{-2} \text{ s}^{-1} \text{ Hz}^{-1} \text{ arcsec}^{-2}$.

The stellar mass densities, gas densities, rotation velocities, gas velocity dispersions, and FUV surface brightnesses were collected from azimuthally-averaged surface photometry and surface density profiles. The intersection of these data sets is 20 galaxies. The widths of the annuli used were fixed for each galaxy, but vary from galaxy to galaxy: 20 pc (IC1613) to 340 pc (DDO 52), with a median over the 20 galaxies of 120 pc. This is the spatial resolution of our study.

The uncertainties in the SED fittings that produce the stellar masses increase as one goes to the outer disk. For example, in CVnIdwA, one of the fainter dwarfs, the last annulus in which we quote a stellar mass density gives the value $\log(M_{\odot} \text{ pc}^{-2}) = -0.88^{+0.24}_{-0.20}$. However, as the uncertainty in the stellar mass climbs, the stellar mass density itself drops and the total mass is dominated by the gas. Therefore, the contribution of the stellar mass uncertainty to the total baryonic mass uncertainty is small. The uncertainty of the FUV surface photometry also increases as the surface brightness drops. We stop when the uncertainty reaches 0.5 mag.

The derivative of the rotation curve at a particular radius, which is used to evaluate the epicyclic frequency κ , was obtained from the difference between the rotation values on either side of that radius. Irregularities in the rotation curves produce irregularities in κ , but they are usually not large. The local values for the derived quantities do not influence the main conclusions here anyway.

3. Two-dimensional gravitational stability at low surface density with a thick disk

Two-dimensional stability in a disk can be measured by the Toomre parameter $Q = \kappa\sigma / (3.36G\Sigma)$ for epicyclic frequency κ , radial velocity dispersion σ , and mass surface density Σ . The factor 3.36

is for a stellar fluid (Toomre 1964); it should be π for a gaseous fluid (Safronov 1960). In a flat rotation curve, $\kappa \sim 1/R$ for galactocentric radius R , and for a typical exponential disk, $\Sigma \propto e^{-R/R_D}$, so that $Q \propto e^{R/R_D}/R$ for nearly constant σ . Such a Q is a decreasing and then increasing function of radius. The increase in the outer part of the disk implies these regions should be stable. More realistic analyses could consider combined gas+star disks, disks with several components of gas at different temperatures, disks with stars plus a highly dissipative turbulent gas, disks with spiral waves that might trigger local gravitational collapse even with a high average Q , etc.

Disk thickness also has an effect. It decreases the in-plane force of gravity per unit mass column density in a disk because the part of the mass that is far from the midplane directs the force vector away from the plane. Vandervoort (1970) showed that in 2D models, the disk mass column density Σ should be decreased by the factor $(1 + kH)^{-1}$ to account for this, where k is the wavenumber (inverse length) of a column density perturbation and H is the disk half thickness. A more detailed study of thickness effects in Elmegreen (2011) confirms this factor and shows that it is accurate to within 12% for a wide range of conditions, compared to a directly integrated force in three dimensions. Because dIrr galaxies and the outer parts of spiral galaxies in general are thought to be relatively thick, there should also be a trend toward greater stability in these regions compared to the conventional 2D analysis just from thickness effects.

The radial profiles compiled for the present survey (Sect. 2) provide good confirmation of these points. Figure 1 shows histograms of the conventional 2D instability parameter $Q = \kappa\sigma/(\pi G\Sigma)$ for gas alone and for stars alone (using π in the denominator for stars too), measured at each radius in each galaxy. Q is generally much larger than unity, which implies stability. Also shown is a histogram of the ratio of the azimuthally-averaged gas surface density to the critical surface density $\Sigma_{\text{crit}} = 0.7\kappa\sigma/(3.36G)$ based on the condition $Q = 1.4$ from Kennicutt (1989). This ratio is low, meaning the disks are stable in a conventional sense, in agreement with the high values of Q for the gas. The Q values are so large that the 2-fluid disk should also be stable, if we consider that the effective Q value is the harmonic sum of the gaseous and stellar values (Wang & Silk 1994). Thickness corrections to this harmonic sum from Romeo & Wiegert (2011) make the disks even more stable in 2D.

Figure 2 shows histograms of the scale heights. These heights are more complicated to calculate than Q because they require a simultaneous equilibrium solution to the vertical distributions of both gas and stars, with the inclusion of forces from dark matter inside the disk (Narayan & Jog 2002). A detailed description of how this is done is in Elmegreen (2011). An assumed dimensionless parameter is the ratio πD of the column densities of dark matter to stars in the center of the galaxy. Other dimensionless parameters are the slope of the rotation curve, called α in that paper, the maximum value of the rotation speed (at large distance) divided by the local stellar velocity dispersion, \hat{v}_{max} , the conventional Q values for stars and gas, the ratio of the velocity dispersions for stars and gas, and the ratio of column densities for stars and gas. The equilibrium solution gives the central densities for stars and gas, and then the scale heights are taken to be half of the ratios of the column densities to the central densities. For this dimensionless calculation, the resulting

scale heights are normalized to the dimension of length, $\sigma_{\text{star}}/\kappa$, which is the half-width of a stellar epicycle in the radial direction. We find that the scale heights do not depend noticeably on D , α and \hat{v}_{max} , after trying a range of values, and so we use $D = 1$, $\alpha = 0.4$, and $\hat{v}_{\text{max}} = 8$ for what follows. For example, the value $\hat{v}_{\text{max}} \sim 5$ for the center of DDO 168 found by Johnson et al. (2015) is consistent with our assumption. The other parameters needed to evaluate the scale heights, as listed above, are taken from the observed radial profiles (Sect. 2).

The histograms in Figure 2 show the distribution of gaseous and stellar scale heights measured in kpc, the ratios of these heights to the local radii, and the ratios of these heights to the local dimensional length, $\sigma_{\text{star}}/\kappa$. Evaluations of these quantities are made at each measured radius for each galaxy. Evidently, the disks are thick in absolute terms ($H_{\text{star}} \sim H_{\text{gas}} \sim 0.5$ kpc), thick when compared to their local radii ($H/R \sim 0.6$) and also thick compared to their local epicyclic radii ($H\kappa/\sigma_{\text{star}} \sim 3 - 5$). This large relative thickness explains the finding by Dalcanton et al. (2004) that dwarf galaxies do not have thin dust layers.

We conclude from Figures 1 and 2 that the dIrr galaxies in our sample are stable by the conventional 2D stability parameter, Q , and that they are relatively thick, making them even more stable than what the large Q values imply. Still, these outer disks form stars with a nearly continuous exponential FUV profile that approximately matches the V-band profile (Hunter et al. 2010). Thus they cannot be so stable. The problem could be the conventional 2D analysis, so we consider first in what follows a more complete 2D model with a realistic equation of state and thickness effects included. We find that this fails to explain the star formation also, so we follow that in Section 5 with a consideration of the 3D problem.

4. Stability analyses for thick two-fluid disks with turbulent energy dissipation

To evaluate the possibility of gravitational instabilities in our sample galaxies, we need to consider the calculated disk thicknesses in addition to the other measured parameters seen in projection. The most complete model for this is the two-fluid instability model in Elmegreen (2011), which also considers the realistic case where the gas is always dissipative with a rate proportional to the crossing time over a perturbation length. This is expected for a supersonic turbulent fluid, and is unlike the case for a thermal or adiabatic fluid which can have an equilibrium unperturbed state. For a turbulent fluid, the gas always dissipates energy unless this energy is re-supplied by either the instabilities themselves, or by the stars that they generate. Prior to the instabilities or star formation, however, the gas is always dissipative.

We follow the analysis in Elmegreen (2011) and calculate the growth rate as a function of wavenumber for each radius in each galaxy, assuming perturbations in a dissipative star+gas mixture, using self-consistent scale heights evaluated as in Section 3. We find that when we use the full scale heights, many disks are so stable for all wavenumbers that the growth time exceeds a Hubble time. To make this point, we show in Figures 3 and 4 a selection of results for the growth

time versus the perturbation scale length (Fig. 3), and the minimum growth time considering all perturbation lengths, versus the radius (Fig. 4). The curves are color coded so that blue curves assume much thinner gaseous and stellar scale heights for the evaluation of the two-fluid growth time than the calculated (true) scale heights, by a factor of 10, the green curves consider scale heights that are 0.4 times the calculated values, and the black curves consider zero-thickness disks as an extreme case. Red curves assume the correct thicknesses, as calculated by the method discussed in Section 3.

In Figure 3, each curve is a dispersion relation, i.e., growth time versus perturbation length, for a single radial annulus in the galaxy indicated. All of the galaxies had dispersion relations like this, to varying degrees, so we only show the results for DDO 50 and DDO 75. Each dispersion relation has a minimum growth time at some intermediate length scale, increasing times for shorter lengths because these are smaller than the disk thickness, and increasing times for longer lengths because of rotational effects. There is no minimum scale for instability (i.e., no threshold Jeans length) in the turbulent-dissipation model. The left-hand panels of Figure 3 show the case where the thickness is forced to be 0.1 times the calculated thickness, the middle panels show 0.4 times the calculated thickness, and the right-hand panels show the correct dispersion relation with the full, self-consistent thickness. All radial annuli are evaluated, although for the $0.4H$ and full-thickness cases, very few annuli have solutions for unstable growth. This means that the actual disks are effectively stable against 2D perturbations.

The shortest growth times regardless of perturbation scale are shown in Figure 4 as a function of radius for all of the galaxies. There are very few red curves, which represent the case where the full thickness is assumed; most of these cases had minimum growth times longer than a Hubble time and are not shown. All galaxies have black curves plotted, which assume the thicknesses are zero, but this is unrealistic. Some have blue curves, which are for 0.1 times the full thickness and still unrealistic. Unstable timescales comparable to a Gyr for ~ 0.5 kpc perturbation scales are shown by the green curves, but even that is somewhat unrealistic as it assumes only 0.4 times the proper thickness.

Figure 5 considers the two-fluid, thick-disk result again, now combined with measures of the SFR, taken to be proportional to the FUV flux density as described above. First, for reference in the left panel, the FUV flux density is plotted versus the gas surface density, showing the usual result for outer disks and dIrr galaxies (Bigiel et al. 2008) that star formation is proportional to the square or higher power of the gas column density. The SFR per unit area scales directly with the FUV flux as shown by the right-hand axis. Each point in the plot is from a different radial annulus in one of the galaxies. The red line is a fit to all of the points and it has a slope of 1.76 ± 0.08 , where the error is the 90% confidence level in a Student t-test. The green line is an average of the fits to each different galaxy; it has a slope of 2.95 ± 2.09 , where the error is the standard deviation of the individual slopes. All of the linear fits in this paper are least squares for ordinate versus abscissa.

The middle panel of Figure 5 shows the ratio of the local gas surface density to the local critical surface density for gravitational instabilities in the usual 2D thin-disk analysis. This ratio is less than 1, as also shown in Figure 1, but now a dependence on the minimum growth time of the local gravitational instability, τ_{GI} , is indicated. This is the same two-fluid, thick-disk instability whose growth time was plotted in Figures 3 and 4. As the growth time increases, the ratio $\Sigma_{\text{gas}}/\Sigma_{\text{crit}}$ decreases, as expected since long growth times correspond to stable conditions. The different colors are again for the different assumptions about thickness used for the instability calculation (black: zero thickness, blue: 0.1H, green: 0.4H, red: full thickness). Again, there are very few red dots and those that are plotted occur only for the largest $\Sigma_{\text{gas}}/\Sigma_{\text{crit}}$ (i.e., the realistically thick disks are stable except for the most unstable cases according to the conventional stability criterion).

Westfall et al. (2014) also examined the dependence of the SFR on the two-fluid Q value, finding an inverse correlation analogous to that shown here: high effective Q corresponds to longer two-fluid growth times in our figure, and thus to slower star formation. They also find that the disks in their sample of late-type galaxies are mostly stable because of thickness effects, like we find here.

The right-hand panel in Figure 5 shows the FUV flux density and Σ_{SFR} again versus a first-guess at what the SFR might be from a theory of two-fluid, thick-disk instabilities, namely, $\Sigma_{\text{gas}}/\tau_{\text{GI}}$ for unstable growth time τ_{GI} . The colors are as before with red showing the realistic case of disks with their full thickness. There is no good correlation between Σ_{SFR} and the simple 2D theory unless the disks have zero thickness (black dots) and then the SFR is about 1% of the theoretical rate. This 1% is interesting because it corresponds to an efficiency of 1% for the conversion of gas into stars at the local dynamical rate (e.g., Krumholz & Tan 2007). However, the assumption of zero thickness is unreasonable. We shall recover this $\sim 1\%$ efficiency in a more realistic, 3D model in the next section.

We conclude from this two-fluid, thick-disk stability analysis that our dIrr galaxies are essentially stable against 2D self-gravitational processes. These processes are usually considered relevant for star formation, as, for example, with the common use of a critical column density or Toomre Q threshold, but our galaxies have what appears to be normal star formation in these regions and yet essentially no 2D instabilities. What this lack of 2D instability really seems to mean is that there are no spiral waves, which are 2D processes, and that star formation is fundamentally a 3D process. We know there are no spiral waves in these galaxies, as they are Irregulars. The 2D gravitational instability as a spiral instability, even considering thick disks, should be considered separately from 3D gravitational processes that may lead to star formation.

Extrapolating a bit further, we infer that there could be an unobserved cold and thin-disk component in these disks where star formation is actually occurring (Sect. 6.4). In this component, gravitational instabilities and other processes involving self-gravity would be much stronger than in the average thick gas disk considered above. Formation of this cold component is a 3D process since it involves cooling, collecting and settling of thick disk gas into a thin cloudy layer. The dynamics

of star formation is probably controlled by gravitational and other forces acting in and on this cold thin component. The Mach number could be low there, even sub-sonic, as in the outer regions of the galaxies modeled by Kraljic et al. (2014). An example of such a cold component would be a relatively thin distribution of cool diffuse clouds, which, because of mutual and self-shielding from background stellar light, convert into molecular form. Mutual gravity and turbulent motions that bring these diffuse H_2 clouds together could then be the triggering process for star formation on timescales of tens of millions of years. For such a process, the unstable growth times shown by the black curves and dots in Figures 4 and 5, which assume zero thickness, would be more relevant than the growth times shown by the red curves and dots, which assume the full thickness of the HI layer given by the observed gaseous velocity dispersions and mass column densities.

5. A three dimensional star formation recipe

The measured surface densities and derived disk thicknesses allow us to calculate the 3D densities for both gas and stars, and therefore the Jeans time, $(4\pi G\rho)^{-0.5}$, or the idealized free-fall time for a uniform sphere, $\tau_{\text{ff}} = (32G\rho/3\pi)^{-0.5}$. Figure 6 shows various comparisons between the SFR and models using τ_{ff} . These are now 3D models because they involve space density for the dynamical rates, not solutions to the 2D growth rates.

The upper left panel of Figure 6 shows the FUV intensity and Σ_{SFR} versus a 3D first-guess model for the SFR, $\Sigma_{\text{gas}}/\tau_{\text{ff}}$, using the observed HI properties for the gas. There is a good correlation with slopes of 1.06 ± 0.04 in the red line, which is for all of the points together, and 1.61 ± 0.58 in the green line, which is the average of all of the slopes for the individual galaxies without any weighting. The errors are as above, from a Student t-test and from the rms scatter in the individual slopes, respectively. The closeness of these slopes to unity implies the surface SFR is tracking the 3D dynamical rate.

The conversion between an approximately squared dependence of Σ_{SFR} on Σ_{gas} and an approximately linear dependence of Σ_{SFR} on $\Sigma_{\text{gas}}/\tau_{\text{ff}}$ implies that the disk thickness is changing systematically with both τ_{ff} and Σ_{gas} . These dependencies are shown in the middle and right-hand panels on the top of Figure 6, where $H_{\text{gas}} \propto \tau_{\text{ff}}$ and $H_{\text{gas}} \propto \Sigma_{\text{gas}}^{-1}$. Note that for equilibrium in an isothermal one-component fluid, $H = \sigma^2/(\pi G\Sigma)$ and $\rho = \Sigma/(2H)$. If $H \propto \Sigma^{-1}$ as in the upper right-hand panel, then $\rho \propto \Sigma^2$ and $\tau_{\text{ff}} \propto \Sigma^{-1}$. This converts Σ^2 as in Figure 5 left, to Σ/τ_{ff} as in Figure 6 top-left. In fact Figure 6 uses fits to the HI thickness involving gravity from gas, stars and dark matter, but the scaling between quantities ends up about the same as in this idealized isothermal model. The physical point is that the empirical star formation law appears to change from approximately linear with gas surface density in the inner parts of spiral galaxies to approximately quadratic in the outer parts of spiral galaxies and in dIrrs because of a general thickening of the disk at low surface densities. This point was also made by Barnes et al. (2012) using observations of spiral galaxies.

The left panel in the middle row of Figure 6 shows the FUV intensity and Σ_{SFR} versus a similar model SFR where now the 3D average local HI gas density used for the free fall time has been replaced by the 3D average local stellar density. The motivation for this replacement comes from observations of the good correlation between the SFR and the stellar surface density (Shi et al. 2011) or stellar volume density (Ostriker et al. 2010; Kim et al. 2013) (see also Fig. 7 below). The fitted lines indicated have slopes of 0.93 ± 0.04 (all points, red line) and 1.31 ± 0.56 (average of individual galaxies, green line), with the error limits defined as before. The correlation is about as good as when the free fall time involves the HI gas density, although there is a little more horizontal scatter in the stellar density case. This similarity for the two cases is because the stellar and HI gaseous densities scale with each other (middle panel, middle row). For this density-density correlation, the indicated fits have slopes of 1.24 ± 0.07 (all points, red line) and 1.63 ± 0.84 (average of individual galaxies, green line). The reason the stellar density scales steeper than linearly with the gas density is that the gas-to-star ratio tends to increase in the outer parts of the disks. Indeed, at the lowest values in the outer disks, the HI gas densities are about 10 times the stellar densities; at the highest values in the inner disks, the HI gas and star densities are about the same.

The right-hand panel in the middle row of Figure 6 plots the FUV intensity versus the gas (red) and stellar (blue) surface densities. The gas values are clearly shifted towards higher values. The dispersion in the correlation is higher for the stars than the gas, suggesting that the physical processes of star formation are determined mostly by the gas, with stars playing a secondary role, such as determining the scale height, radiation field, etc.

The bottom-left panel shows the ratio of the observed SFR, calculated as before from the azimuthally-averaged FUV intensity, to the 3D first-guess SFR, calculated as before from the ratio of the azimuthally-averaged HI gas surface density to the 3D free fall time. This ratio has become known as the efficiency of star formation per unit free-fall time, ϵ_{ff} , considering a star formation law where the SFR per unit area equals $\epsilon_{\text{ff}} \Sigma_{\text{gas}} / \tau_{\text{ff}}$ (Elmegreen 2002; Krumholz et al. 2009a, 2012). All of the points cluster around a nearly constant efficiency that is within a factor of three of 1%. The actual average in the figure is $\log_{10} \epsilon_{\text{ff}} = -1.99$, which corresponds to $\epsilon_{\text{ff}} = 1.0\%$.

The efficiency is shown again in the middle panel of the bottom row of Figure 6, with one point for each radial annulus in each galaxy, but now spread out along the abscissa so that radial trends can be seen. The plot moves from left to right with increasing radius and from one galaxy to the next. There is an increasing segmented line showing the jumps from one galaxy to another; i.e., the segmented line is horizontal inside each galaxy and then increments upward by one unit for the next galaxy. The order of the galaxies is the same as in Table 1. The scatter in efficiency in the bottom-middle panel is the same as in the bottom-left panel, as the ordinate values are exactly the same, but now a trend appears such that within each galaxy, the points show a systematic decrease with increasing radius.

These radial decreases in efficiency are shown again in the bottom-right panel where each galaxy is now plotted as a separate curve, normalized in radius to the V-band scale length, R_{D} .

There is clearly a systematic dependence of ϵ_{ff} on R/R_{D} ; the average trend is given by the red curve. The left-hand axis for this plot has the log of ϵ_{ff} with a base-10 logarithm, while the right-hand axis has $\ln \epsilon_{\text{ff}}$ with a natural log. The two black straight lines in the bottom-right panel are drawn to guide the eye; they have slopes of -1 and -0.5 using the natural log axis, as labeled. The average fitted slope of -0.54 is given by the black dotted curve. The trend in $\ln \epsilon_{\text{ff}}$ versus R/R_{D} has a slope of about -0.5 , which means that ϵ_{ff} decreases exponentially with radius in proportion to the square root of the V-band surface brightness, which would have a slope of -1 on such a plot (e.g., see Figure 8 below). In other words, ϵ_{ff} is exponential with a scale length that is about twice the scale length of the optical disk. An exponential decrease in the efficiency with radius was also shown by Yim et al. (2014) for four spiral galaxies. In the next section, we discuss a possible origin for the radial dependence of the efficiency of star formation.

The dependence of the SFR on the surface density of stars deserves another look. Shi et al. (2011) find a good correlation with $\epsilon_{\text{ff}} \propto \Sigma_{\text{star}}^{0.5}$. We show the analogous dependency for our galaxies in Figure 7. This differs from the left panel in the middle row of Figure 6, because that uses $1/\tau_{\text{ff}} \propto \rho_{\text{star}}^{0.5}$ on the abscissa instead of Σ_{star} . The correlation in Figure 7 is steeper than the Shi et al. correlation, with an average slope of 0.76, as shown by the dashed red line. However, if we consider only the low surface brightness and late-type galaxies in Shi et al. (2011), which are most similar to our galaxies, then their correlation with Σ_{star} is also steeper than their derived average slope of 0.5. Consider the LSB and late-type points in their Figures 1 and 3, and especially their Figure 5, which is the combined result for 12 of their spiral galaxies. Their plotted points for those galaxies, ie., for the lowest SFR galaxies in their Figure 5, have a steeper slope than all of the points combined, and steeper than their least-squares fit to all of the points. The slope for the low-SFR points in their Figure 5 is closer to 1 than 0.5, and in approximate agreement with the slope we find here in Figure 7. Thus our data agree approximately with the THINGS data used in Shi et al. (2011).

6. Radial variation of the efficiency as an indicator of varying molecular fractions

6.1. Radial variations

The 3D star formation model used in the previous section,

$$\Sigma_{\text{SFR}}(R) = \epsilon_{\text{ff}}(R)\Sigma_{\text{gas}}(R)/\tau_{\text{ff}}(R), \quad (1)$$

contains the quantity Σ_{gas} that has been set equal to the HI column density. Considering the measured value of $\epsilon_{\text{ff}} \sim 1\%$, the implication of this equation is that approximately 1% of the HI gas turns into stars per unit free fall time as measured at the average midplane density of HI. Of course, stars are not forming at the average midplane HI density; they form in denser clouds. Nor is the free fall time in the star-forming gas as long as the free fall time at the average density; stars form in dense molecular gas on much shorter local timescales (discussed below in Sect. 6.4).

To get some sense of the values and radial trends for the gaseous and stellar surface densities, 3D space densities, and scale heights, Figure 8 plots these quantities using a separate curve for each galaxy. The plots use a natural logarithm on the ordinate and a linear normalized radial scale on the abscissa, so that the slopes of the curves can be readily identified in relation to the exponential light profiles, which all have slopes of -1 , by definition. Each panel also shows fiducial slopes of -1 and -0.5 as straight lines, and in the cases of 3D stellar density and FUV flux, -1.5 , as labeled. The average trends are summarized in Table 2, which gives the natural log of the central value (“V”) for comparison to the figure, the physical values at the center and at $4R/R_D$, and the exponential factor, which is the slope in the figure. Standard deviations come from the galaxy-to-galaxy variation. Table 2 also gives the average radial variation of gas velocity dispersion from the HI observations and the derived quantity τ_{ff} .

There are clear trends shared by these galaxies. The stellar surface density profile (top middle) has a slope of about -1 , showing essentially the exponential disk as viewed in the V-band (although the surface density was determined from SED fitting). The stellar and gaseous scale heights (top and middle right-hand panels) are similar to each other and both increase with radius about as $\exp(0.5R/R_D)$. The stellar volume density therefore decreases with radius as $\exp(-1.5R/R_D)$, from $\Sigma_{\text{star}}/H_{\text{star}}$, as shown in the top left panel. This rapid decrease of stellar density corresponds to a similar decrease in volume emissivity for V-band stellar light, j_V , and it occurs throughout the entire radial range in most of the disks; volume emissivity does not follow the projected radial profile but is steeper because of the steady increase with radius in the disk thickness.

The surface density of HI gas follows a shallower trend than the surface density of stars, being more like $\exp(-0.5R/R_D)$. Thus the 3D HI density varies as $\Sigma_{\text{gas}}/H_{\text{gas}} \propto \exp(-R/R_D)$, as shown in the middle left panel. The absorption coefficient from dust, κ_a , is proportional to the gas density for constant metallicity (as observed in dIrrs; Pagel et al. 1980; Roy et al. 1996; Kobulnicky & Skillman 1996, 1997), so it should also follow the $\exp(-R/R_D)$ trend. As a result, the local radiation field in V-band, $\langle \Phi_V \rangle$ does not mimic the projected light distribution, which would be $\exp(-R/R_D)$, but rather $\langle \Phi_V \rangle \sim j_V/\kappa_a \sim \exp(-0.5R/R_D)$, which has twice the scale length. Local radiation fields are higher in the outer parts of these galaxies than the projected light profiles suggest. Similarly, the local gas density drops faster with radius than the observed column density.

On the bottom left of Figure 8 is the FUV flux density and Σ_{SFR} versus radius in a plot of the natural-log versus R/R_D . This panel shows a variation of the areal SFR that is proportional to the power 1.5 of the V-band surface brightness, i.e., the slope is -1.5 on that plot. Thus the volume emissivity of the SFR scales as $\exp(-2R/R_D)$, considering the H_{star} variation. In the bottom central panel is the ratio $n_{\text{star}}/n_{\text{gas}}$, which is proportional to the ratio of the V-band volume emissivity, j_V , to the absorption coefficient from dust, κ_a ; it scales with the square root of the V-band surface brightness.

This difference between local radiation field and surface brightness calls into question an assumption of the star formation models in Ostriker et al. (2010), Kim et al. (2013), and Krumholz

(2013), which was that the local radiation field follows the SFR per unit area. As mentioned above, the radiation field in V-band is approximately $\langle \Phi_V \rangle \sim j_V / \kappa_a$ where $j_V \propto \Sigma_{\text{star}} / H_{\text{star}}$ and $\kappa_a \propto \rho_{\text{gas}} \propto \Sigma_{\text{gas}} / H_{\text{gas}}$ for small metallicity gradient. Thus $\langle \Phi_V \rangle \propto \Sigma_{\text{star}} H_{\text{gas}} / (\Sigma_{\text{gas}} H_{\text{star}})$. But $H_{\text{gas}} \propto H_{\text{star}}$ from Figure 8, thus $\langle \Phi_V \rangle \propto \Sigma_{\text{star}} / \Sigma_{\text{gas}}$ which is shallower than Σ_{star} alone. Similarly, in FUV, $\langle \Phi_{\text{FUV}} \rangle \propto j_{\text{FUV}} / \kappa_a \propto \exp(-R/R_D)$ which is shallower than $\Sigma_{\text{SFR}} \propto \exp(-1.5R/R_D)$. Also in a study of 17 spirals and 5 dIrrs in the THINGS survey (Bigiel et al. 2010), Σ_{gas} and the intensity of FUV both vary approximately exponentially in the outer parts, with a generally shallower slope for Σ_{gas} than FUV; thus the local radiation field should be shallower than the FUV profile for the THINGS galaxies too.

The bottom right panel of Figure 8 shows the natural logarithm of the ratio $\Sigma_{\text{gas}} / \tau_{\text{ff}}$ versus normalized radius. There is a direct scaling with the V-band (i.e., the slope is about -1). This direct scaling also follows from the middle panels Figure 8 considering that $\tau_{\text{ff}} \propto \rho_{\text{gas}}^{-1/2}$, because in the middle-center panel, $\Sigma_{\text{gas}} \propto \exp(-0.5R/R_D)$ and in the left-center panel, $\rho_{\text{gas}} \propto \exp(-R/R_D)$. The ratio of the plotted quantities in the bottom left and right-hand panels is the efficiency, plotted in the lower right of Figure 6. This ratio has the residual dependence on $\exp(-0.5R/R_D)$ as shown in Figure 6 because the SFR profile is steeper than the purely dynamical profile given by $\Sigma_{\text{gas}} / \tau_{\text{ff}}$ for HI. The residual variation could be from the molecular fraction, as discussed in the next section.

We note that the radial variation of the disk density from stars and dark matter, usually dominated by stars, is not considered in Krumholz (2013), which is a study of star formation at low HI surface density, as is the present paper. This quantity, called ρ_{sd} in that paper, is taken to be constant for all gas surface densities, Σ , in their theoretical Kennicutt-Schmidt plots of Σ_{SFR} versus Σ_{gas} , when in fact all three quantities, Σ_{SFR} , Σ_{gas} and ρ_{star} vary with radius for the galaxies studied here. That is, ρ_{star} varies as approximately the 3rd power of Σ_{gas} in the radial direction.

An interesting feature of the radial dependencies for $\Sigma_{\text{gas}}(\text{HI})$ and $n(\text{HI})$ is that $n(\text{HI})$ is proportional to the total interstellar pressure, P . This is because $P \sim \pi G \Sigma_{\text{gas}}^2 / 2$ for our gas-dominated disks and $\Sigma_{\text{gas}} \propto \exp(-0.5R/R_D)$ from Figure 8. Thus $P \propto \exp(-R/R_D)$, and this is also proportional to $n(\text{HI})$, from Figure 8.

6.2. Molecular diffuse clouds

The average midplane HI gas densities in our dIrr disks are rather low, with values of $\exp(-1.5) = 0.2 \text{ cm}^{-3}$ starting in the center and then decreasing outward (middle row, left panel in Fig. 8). This implies that the gas is generally tenuous, much more so than in the local solar neighborhood. Still, the gas is probably cloudy with the observed HI only an average over clouds inside the HI resolution limit and spread out around a radial annulus. The denser parts of these clouds and those shielded from radiation could be partially molecular, although not necessarily self-gravitating. We refer to non-self-gravitating clouds as diffuse.

“Standard” diffuse clouds in the solar neighborhood are mostly H_2 (Hollenbach et al. 1971;

Spitzer & Jenkins 1975; Jura 1975); CO is not observed from them in emission although some CO is observed in absorption (Federman et al. 1980). To some extent, clouds in the solar neighborhood shield each other from H₂ dissociating radiation; to them, a large fraction of the sky is nearly black in the Lyman-Werner bands unless an early type star is closer than the standard cloud mean free path, which is about 100 pc. The top panel of Figure 9 shows a typical spectrum of a nearby hot star in an H₂ absorption line, from Spitzer & Jenkins (1975). The line center flux is effectively zero, so no photo-dissociating radiation from this transition gets through the intervening clouds to us.

Evidence for diffuse H₂ was shown in a study of dust and HI emission from the Perseus region (Lee et al. 2012, see also Barriault et al. 2010). The middle panel of Figure 9 illustrates this region of the sky and the bottom panel shows the probability distribution function (pdf) of K-band extinction, both from Lombardi et al. (2010). Superposed on the extinction distribution is the threshold for H₂ formation determined by the Copernicus satellite in the 1970’s (Spitzer & Jenkins 1975), namely, $A_V > 0.3$ mag for the solar neighborhood ($A_K > 0.033$ mag in K-band). This extinction threshold corresponds to a mass surface density threshold $\Sigma \sim 5.9 M_\odot \text{ pc}^{-2}$, and is reproduced by the theory of H₂ formation (e.g., Hollenbach et al. 1971; Jura 1975; Krumholz et al. 2009b; Sternberg et al. 2014). Also shown in the figure is the threshold for CO formation, which is approximately $A_V \gtrsim 1.5$ mag ($A_K > 0.165$ mag) in the solar neighborhood (Federman et al. 1980; Pineda et al. 2008). Note the gray-scale bar on the right in the middle panel. The blue horizontal bar near the bottom of it indicates the gray scale threshold for H₂ formation. Most of the image is darker than this, suggesting that molecular diffuse clouds nearly cover the field. Considering also the CO threshold, a small fraction of the area is likely to contain CO, although most of it contains H₂.

A similar situation but more extreme compared to that in the solar neighborhood arises in dwarf Irregular galaxies where low metallicities make CO hard to form and detect but significant amounts of H₂ are inferred anyway from a high abundance of dust without the usual accompaniment of HI (Leroy et al. 2008; Hunt et al. 2010; Bolatto et al. 2011; Elmegreen et al. 2013; Shi et al. 2014; see review in Bolatto et al. 2013).

The formation of H₂ in giant molecular clouds (GMCs) can be more easily understood if GMCs are collections of diffuse H₂ clouds. If the H₂ forms before the GMCs, then there is no problem with slow molecule formation like that discussed by Mac Low & Glover (2012). The gas could spend a relatively long time in the diffuse phase forming H₂ if the conditions are right, and then convert back to HI after the GMC phase, when star formation breaks the clouds apart. Molecule formation should not only be a *self*-shielding process for individual clouds, but also a *mutual* shielding process for collections of clouds shielding each other (Elmegreen 1993). Other discussions of diffuse molecular clouds are in Elmegreen (2013) and Shetty et al. (2013, 2014).

For reference, the local threshold column density for star formation discussed by Lada et al. (2010) and Evans et al. (2014) is also shown in Figure 9. It is $A_K > 0.8$ mag, or $A_V > 7.3$ mag, or $\Sigma_{\text{gas}} > 145 M_\odot \text{ pc}^{-2}$ including He and heavy elements at solar metallicity.

The low gas densities in our dIrr sample suggest that most of the interstellar medium is a mixture of warm and cool HI, with a non-negligible but small fraction of the mass in molecular form. Most of these molecules are probably diffuse, also because of the low average density, with sparsely distributed cores in which gravity is strong and stars form. In that case, the molecular fraction can be determined in some average sense by an equilibrium between H₂ formation at the root mean squared density, and H₂ destruction at the mean density in the local average radiation field. This is a different model than determining the transition from atomic to molecular gas at the edge of a single dense cloud, and also different from determining the average molecular fraction from the fraction of the gas mass in the form of isolated dense molecular clouds, which may have applications elsewhere (e.g., Krumholz et al. 2009b). We return to this point in Section 6.5.

The equilibrium may be written approximately as

$$n(HI)n(\text{dust})R_{\text{form}} = n(H_2)f_{\text{diss}}\Phi\sigma_{\text{dis}} \quad (2)$$

where R_{form} is the formation rate of molecules on dust (e.g., Hollenbach et al. 1971; Jura 1975), Φ is the local radiation field and σ_{dis} is the cross section for H₂ dissociation in the radiation field (which includes the fraction of absorptions leading to dissociation). Equation 2 is analogous to equations (37)-(38) in McKee & Krumholz (2010), who consider an additional average over radiation frequency. If $n(H_2) \ll n(HI)$ on average, then

$$\frac{n(H_2)}{n(HI)} \sim \frac{n(HI)D_{\text{DTG}}R_{\text{form}}}{\Phi\sigma_{\text{dis}}} \propto \frac{n(HI)(Z/Z_{\odot})}{\Phi} \quad (3)$$

for dust-to-gas ratio D_{DTG} and metallicity dependence Z from the dust. We expect that the efficiency of star formation, ϵ_{ff} , contains a dependence on $n(H_2)/n(HI)$, which effectively converts the Σ_{gas} from HI observations into a local molecular column density. This is because most star formation occurs in molecular gas even at low average density and moderately low metallicity (Wong & Blitz 2002; Krumholz et al. 2011). Since we measure the radial distribution of $n(HI)$, we need to evaluate the radial distribution of the radiation field Φ in order to compare the expected molecular fraction from equation (3) with the observation of $\epsilon_{\text{ff}}(R)$. A more complete theory would also consider the distribution function of diffuse cloud column densities and the discrete nature of the brightest radiation sources.

Equation (3) is similar to the result in Elmegreen (1993) where, following a more detailed model, the molecular fraction at low molecular fraction, in a combined diffuse and self-gravitating medium, was written as approximately $P^{2.2}/j$ for interstellar thermal pressure P . The similarity arises because $P \propto n(HI)$ for constant diffuse cloud temperature and because volume emissivity $j \propto \Phi\kappa_a \propto \Phi n(HI)$ for constant metallicity.

6.3. Radiative transfer in the diffuse interstellar medium of dIrr disks

We would like to evaluate the radial distribution of the radiation field in our dIrr galaxies, given the observed and derived radial distributions of the HI and stellar densities and the derived

scale heights. We do this by solving the integral form of the equation of radiative transfer,

$$I(\theta, \phi, R_O) = \int_0^{s_{\max}} j(s) e^{-\tau(s)} ds \quad (4)$$

where optical depth is

$$\tau(s) = \int_0^s \kappa_a(s') ds' \quad (5)$$

for variables s and s' along a sightline in the direction (θ, ϕ) , where θ is the polar angle with respect to the z direction at the position of the observer (subscript “O”) at galactocentric radius R_O , and ϕ is the azimuthal angle measured by the observer around the disk starting at the direction to the galactic center. The volume emissivity and absorption coefficient depend on position in the galaxy. For the V-band emission,

$$j_V(R, z) = \exp(-1.5R/R_D - z/H_{\text{star}}) \quad , \quad \kappa_a(R, z) = \kappa_0 \exp(-R/R_D - z/H_{\text{gas}}). \quad (6)$$

Here we have used two profiles from Figure 8, the HI density profile for the absorption coefficient and the stellar density profile from the V-band. The HI density profile is a good representation of the absorption κ_a if the dust is not confined to dense tiny clouds (much smaller than the HI angular resolution). Such dense clouds can have a long physical mean free path. The ratio of the physical mean free path between clouds to the photon mean free path for dust absorption, $1/\kappa_a$, is the intrinsic dust opacity of each cloud, τ_{cl} . If the intrinsic opacity is small, then photons travel through many clouds before they get absorbed on dust and the average density from HI is relevant for κ_a . However, the use of $\kappa_a \propto n(\text{HI})$ does not necessarily assume that all of the absorption is by dust. The real assumption is that the average radiation field in a local volume containing many clouds varies with galactocentric radius as if the total opacity from dust and molecules is proportional to $n(\text{HI})$. The molecular fraction and equation (2) then refer to average formation and dissociation rates among all clouds inside this local volume. It could still be that some clouds are more molecular than others depending on density and opacity.

We also consider a second model that uses the FUV volume emissivity profile $j_{\text{FUV}} \propto \exp(-2R/R_D - z/H_{\text{star}})$ from the FUV flux density in Figure 8 divided by H_{star} . The FUV is more appropriate for H_2 dissociation, but if other factors are important, such as thermal heating, cosmic ray flux, or stellar mass, then the V-band profile might be relevant too.

We are interested in the radial trends, so the volume emissivities are normalized to the values at the galactic center. The scale heights are also assumed to vary with radius, as observed in Figure 8,

$$H_{\text{gas}} \sim 400e^{0.5R/R_D} \text{ pc} \quad ; \quad H_{\text{star}} \sim 400e^{0.5R/R_D} \text{ pc}. \quad (7)$$

The central absorption coefficient, $\kappa_a(R=0)$, is given by the relation

$$2H_{\text{gas}}(R=0)\kappa_a(R=0) = \ln(10^{0.4A_V[R=0]}) \quad (8)$$

where the visual extinction in the center, $A_V(R=0)$, comes from the total hydrogen column density there, N , as $A_V = N/1.87 \times 10^{21}$, using $E(B-V) = N/5.8 \times 10^{21}$ from Bohlin et al. (1978) with a

ratio of total to selective extinction $R = 3.1$. Considering that A_V/N should scale with metallicity Z ,

$$A_V(R = 0) = \Sigma_{\text{gas}}(R = 0)(Z/Z_{\odot})/(1.87 \times 10^{21} \mu). \quad (9)$$

We evaluate κ_a at the center assuming $\ln \Sigma_{\text{gas}} = 2$ at the center, from the center-middle panel of Figure 8, and using a mean molecular weight of $\mu = 2.2 \times 10^{-24}$ g. We also assume $Z/Z_{\odot} = 1/8$ which is about the average for our dIrr galaxies. This gives a central photon mean free path for visible light of $1/\kappa_a = 18.4$ kpc. Considering also that $A_{\text{FUV}} = 8.24E(B - V) = 2.6A_V$ from Cardelli et al. (1989), the central absorption coefficient in FUV corresponds to $1/\kappa_{\text{FUV}} = 7.1$ kpc. The radial scale length in V-band, R_D , is taken equal to the average for our 20 galaxies, which is 740 pc, using the photometry and distances in the LITTLE THINGS survey (Hunter et al. 2012).

The galactic cylindrical coordinates (R, z) are related to s, θ , and ϕ from the point of view of the observer by the equations

$$R = \left([s \sin \theta \cos \phi - R_O]^2 + [s \sin \theta \sin \phi]^2 \right)^{0.5}; \quad z = s \cos \theta. \quad (10)$$

This is enough to give the intensity in all directions at radius R_O . The average radiation field is then the integral,

$$\Phi(R_O) = \frac{1}{4\pi} \int_{-\pi}^{\pi} \sin \theta d\theta \int_0^{2\pi} d\phi I(\theta, \phi, R_O). \quad (11)$$

The integrals (4), (5), and (11) were evaluated numerically with enough resolution in all coordinates s, θ , and ϕ , to obtain convergence. The integral over the line of sight, s , had a limit in galactocentric radius, R , of 20 scale lengths and a limit in the vertical direction, z , of 6 times the local scale height for stars.

The results of this integral are used for the evaluation of mean molecular fraction in equation (3), where Φ occurs in the denominator beneath the gas density $n(\text{HI})$. If the residual radial trend in the star formation efficiency per unit free fall time, ϵ_{ff} , is the result of variations in the mean molecular fraction, then the curves in the lower right of Figure 6 should follow the trend given by equation (3). Thus we plot $n(\text{HI})/\Phi$ in that figure. The green dashed curve is for V-band light with $j_V \propto \exp(-1.5R/R_D)$ and $1/\kappa_a(R = 0) = 18.4$ kpc, and the red dashed curve is for FUV light with $j_{\text{FUV}} \propto \exp(-2R/R_D)$ and $1/\kappa_{\text{FUV}}(R = 0) = 7.1$ kpc. The curves are scaled arbitrarily in the vertical direction. The FUV curve is flatter than the V-band curve because the volume emissivity is steeper in FUV than in V-band. Both curves are nearly flat in the center because the mean free path there is larger than the radius, so an observer would see through to the other side of the galaxy where the emissivity is low.

The radiative transfer solution in Figure 6 follows the trend of the efficiency, ϵ_{ff} when the V-band light is used for the molecular fraction (green dashed curve). In this case, the SFR is proportional to the product of three quantities: the available HI gas mass, the 3D gravitational rate measured at the midplane density of HI, and the diffuse molecular fraction, which is assumed proportional to the ratio of the gas density to the V-band radiation field. This star formation

law is fairly simple, but dIrr galaxies may be simple too: gas dominates stars in mass, extinction is weak, the molecular fraction may be low, and the disk is too thick to support 2D instabilities like spiral waves. The dependence on 3D density does not indicate a particular star formation mechanism; many mechanisms have a characteristic timescale proportional to the average self-gravity time, including gas collapse in expanding shells, collapse following turbulence compression, and 3D gravitational instabilities in the ambient medium (Elmegreen 2002).

6.4. Solutions with the FUV radiation field: what they mean about the H₂ layer

The red dashed curve in Fig. 6 uses the FUV radiation profile and the result is a nearly constant ϵ_{ff} with radius. The constant $n(\text{H}_2)/n(\text{HI})$ in this case follows from equation (3) with $\Phi_{\text{FUV}} \approx j_{\text{FUV}}/\kappa_{\text{FUV}}$ if we use the observation in the bottom left panel of Figure 8 that the FUV flux density $\propto \exp(-1.5R/R_{\text{D}})$ and continue to use $H_{\text{star}} \propto \exp(0.5R/R_{\text{D}})$, which gives $j_{\text{FUV}} \propto \exp(-2R/R_{\text{D}})$. Taking κ_{FUV} proportional to $n(\text{HI}) \propto \exp(-R/R_{\text{D}})$ as before then gives $\Phi_{\text{FUV}} \propto \exp(-R/R_{\text{D}})$. Thus $n(\text{HI})/\Phi$ in equation (3) is independent of radius.

This result suggests an interesting possibility if we again match the observed radial profiles, but now use j_{FUV} for the evaluation of the molecular fraction. Considering only the H₂ layer as a determinant of the SFR, the areal SFR is

$$\Sigma_{\text{SFR}} = \epsilon_0 \Sigma_{\text{gas}}(\text{H}_2) / \tau_{\text{ff}}(\text{H}_2), \quad (12)$$

where $\Sigma_{\text{gas}}(\text{H}_2)$ is the column density of H₂, $\tau_{\text{ff}}(\text{H}_2) = (32G\rho[\text{H}_2]/3\pi)^{-0.5}$ is the free-fall time at the average H₂ density, and ϵ_0 is a constant. In this interpretation, the molecular gas is made explicitly relevant for star formation, rather than through a molecular fraction proportional to ϵ_{ff} as above.

Now we have to imagine what the H₂ clouds are like in order to derive $n(\text{H}_2)/n(\text{HI})$. They should still be mostly diffuse except for occasional self-gravitating cores where stars form, because the interstellar gas density is low on average. Presumably the cores contain CO molecules. Equation (2) should apply to most regions, but now we might consider a non-negligible molecular fraction, which, after solving, becomes

$$\frac{n(\text{H}_2)}{n(\text{HI})} \sim \frac{1}{\Phi \sigma_{\text{dis}} / n(\text{HI}) D_{\text{DTG}} R_{\text{form}} - 2}. \quad (13)$$

This equation was obtained by setting $n(\text{dust}) = (n(\text{HI}) + 2n(\text{H}_2)) D_{\text{DTG}}$. In the previous solution, $\Phi \sigma_{\text{dis}} / n(\text{HI}) D_{\text{DTG}} R_{\text{form}} \gg 2$ so $n(\text{H}_2)/n(\text{HI}) \ll 1$. Now with $\Phi_{\text{FUV}}/n(\text{HI})$ approximately constant with radius, $n(\text{H}_2)/n(\text{HI})$ is still constant, and equation (13) allows it to be unity or larger.

A constant or high molecular fraction seems out of place for dIrr galaxies, where CO has barely been detected yet. However, there is growing evidence that H₂ might be much more abundant than

we have been expecting. Leroy et al. (2008) hinted at this given the high SFR per unit HI in dIrrs, and there is also direct evidence for substantial far-infrared emission and dust, which implies a high gas content, even when the HI emission is low, as referenced in Section 6.2 (see review in Bolatto et al. 2013).

The next step is to consider what the profile of $\Sigma_{\text{gas}}(H_2)$ might be, as that involves the scale height of the molecular layer in addition to the 3D density, $n(H_2)$, which comes independently from equation (2). Here we call upon an important difference between cool HI and H_2 : the atomic gas has a warm thermal phase that maintains a high (thermal) velocity dispersion and a large scale height. Cool HI clouds forming by thermal instabilities in the warm HI layer can appear at any height where the local pressure supports two thermal phases. In this sense, the scale height of cool diffuse HI clouds is not directly the result of some driven turbulent speed, but more the result of the thermal speed of the warm HI, from which the clouds condense and fall down. Such falling could be a source of turbulence in the cool HI medium. The H_2 layer is different because it has no pervasive and warm thermal phase from which cool H_2 clouds condense. H_2 forms where the cool HI is shielded from starlight. The molecular clouds can be confined to the midplane for example, with arbitrarily low turbulent speed and correspondingly thin line-of-sight depth. The thickness of the H_2 layer could be the result of opacity combined with turbulence and direct stirring, since the thermal speed of H_2 is low.

With this in mind, we consider that the H_2 layer thickness does not flare as much as the HI layer, so that $\Sigma_{\text{gas}}(H_2)$ scales almost directly with $n(H_2)$, i.e., as $\exp(-R/R_D)$. Recall, that this is the radial dependence of $n(HI)$ from Figure 8 and $n(H_2)/n(HI) \sim \text{constant}$ in our model with FUV irradiance. A thin sub-layer of H_2 in the midst of a flaring layer of HI does not violate our assumptions in deriving the molecular fraction, since only the average midplane density of $n(HI)$ was used. Also, the opacity in our galaxies is so low, with optical depths larger than any of these thicknesses, that the vertical distribution of the gas does not much affect the radiation field Φ .

What it means physically for $\Sigma_{\text{gas}}(H_2)$ to be proportional $n(H_2)$ is that there is a constant number of H_2 clouds per line of sight through a galaxy, whereas with $\Sigma_{\text{gas}}(HI)$ proportional to $n(HI)H_{\text{gas}}$, the number of standard HI clouds per line of sight increases with radius as H_{gas} increases. The H_2 clouds can be at any height above the plane, i.e., they do not have to be exactly in the midplane, but they need a total thickness that is approximately independent of radius. Stars forming in the H_2 clouds should have the same range of heights as the clouds, possibly filling the stellar scale height H_{star} after 100 Myr, which is the stellar age range observed in the FUV band.

This model gives the radial dependence of the FUV and SFR, $\exp(-1.5R/R_D)$, as observed in Figure 8, using the molecular form of the SFR, equation (12), because

$$\Sigma_{\text{gas}}(H_2) \propto n(H_2) \propto n(HI) \propto e^{-R/R_D} \quad (14)$$

and

$$1/\tau_{\text{ff}}(H_2) \propto n(H_2)^{0.5} \propto n(HI)^{0.5} \propto e^{-0.5R/R_D}. \quad (15)$$

This model also gives $\Sigma_{\text{gas}}(H_2)/\Sigma_{\text{gas}}(HI) \propto \exp(-0.5R/R_D)$ as before (this was ϵ_{ff} in the model of Section 6.1), but now it is from $H(H_2)/H_{\text{gas}}(HI)$ with constant H_2 layer thickness. Before, $n(H_2)/n(HI)$ varied with radius this way, with $H(H_2) \propto H(HI)$. Thus in both cases, the integrated molecular fraction decreases with radius with twice the V-band scale length, but when the FUV band determines the 3D molecular fraction, the local molecular fraction in the region of the H_2 clouds is about constant with radius. Also in both cases, the density used for the dynamical time, $n(HI)$ in Section 6.3 and $n(H_2)$ in the present section, is proportional to total interstellar pressure as determined from the column density.

6.5. Avoiding a sharp transition in the molecular fraction of the ISM

The inferred variations of FUV volume emissivity, $j_{\text{FUV}} \propto \exp(-2R/R_D)$, and midplane gas density, $n(HI) \propto \exp(-R/R_D)$, produce a ratio $j_{\text{FUV}}/n(HI)^2$ that is constant with radius. If we continue to identify the local radiation field, Φ , with $j_{\text{FUV}}/\kappa_{\text{FUV}}$ and if $\kappa_{\text{FUV}} \propto n(HI)$, then $\Phi/n(HI)$ is constant. This is the primary assumption made by Krumholz et al. (2009a,b) in their derivation of molecular self-shielding in clouds. With this assumption, the ISM can maintain two thermal phases and cool HI clouds are possible. This is an important aspect of our model also because cool HI clouds are the source of molecules and eventual star formation even in a diffuse molecular medium.

If we consider molecule formation on a cloud-by-cloud basis, which means that clouds are either highly molecular beyond some column density threshold or highly atomic below this threshold, then we would obtain a certain variation of average molecular fraction with galactocentric radius that may be compared with the observations. In Krumholz et al. (2009b), such an assumption produces a sharp radial transition in the overall molecular fraction of the ISM, and this sharpness is offered as an explanation for the break in the slope of the star formation – column density relation between the inner and outer disks (see Section 1). A sharp transition is inconsistent with the smooth variations in FUV and gas properties that are observed in our dwarf galaxy sample here.

To be more specific, we consider two examples. We first model the formation of molecules according to equation (2), which may be re-written in terms of a threshold column density for individual clouds to shield themselves and form H_2 . Writing this threshold as $\Sigma_{\text{thresh}} = (n(HI) + 2n(H_2))L$ for cloud depth L , we obtain

$$\Sigma_{\text{thresh}} \sim \frac{\Phi}{n(HI)R_{\text{form}}D_{\text{DTG}}}, \quad (16)$$

where $n(H_2)\sigma_{\text{dis}}L \sim 1$ at the threshold because this is the optical depth for self-shielding. If $\Phi/n(HI) \sim \text{constant}$ with radius in the FUV case, then the shielding threshold is also about constant. The column density for shielding is about constant in the model by Krumholz et al. (2009b) too, as given by their equations (12) or (49) and their Figure 4 at high Σ_{obs} , because they also have a constant ratio of photon to gas density.

To see the implications of the shielding layer on a population of clouds, we set the radial profile of the molecular fraction in a galaxy equal to the radial profile of the mass fraction of all of the shielded parts of clouds. Clouds with column densities greater than Σ_{thresh} are assumed to have the excess column density in molecular form and the rest atomic, while clouds with $\Sigma < \Sigma_{\text{thresh}}$ are assumed to be totally atomic. This means that as the pdf for cloud column density (Fig. 9) shifts toward lower mean values with increasing radius, the integral above Σ_{thresh} of the pdf multiplied by $\Sigma - \Sigma_{\text{thresh}}$, which is the molecular part, decreases also. The log-normal form of this pdf causes the integral to drop abruptly at some radius.

The molecular fraction in this threshold model is given by

$$\frac{n(H_2)}{n_{\text{total}}} = \frac{\int_{\Sigma_{\text{thresh}}}^{\infty} (\Sigma - \Sigma_{\text{thresh}}) P(\log \Sigma) d \log \Sigma}{\int_0^{\infty} \Sigma P(\log \Sigma) d \log \Sigma} \quad (17)$$

where

$$P(\log \Sigma) = P_0 e^{-0.5(\log \Sigma / \Sigma_{\text{peak}})^2 / S^2}. \quad (18)$$

The dispersion S is usually written in terms of an effective average Mach number (Padoan, Nordlund & Jones 1997), M ,

$$S = (\ln(1 + 0.25M^2))^{0.5}, \quad (19)$$

and the column density at the peak is proportional to the average column density of clouds,

$$\Sigma_{\text{peak}} = \Sigma_{\text{ave}} e^{-0.5S^2}. \quad (20)$$

The radial variation of Σ_{ave} is not known as this is for individual clouds rather than for the whole ISM, which is what we measure directly. We assume in two models that it varies either as the observed HI column density, which is approximately $\propto e^{-0.5R/R_D}$ in the star-forming region (Sect. 6.1 and Table 2), or as the inferred HI midplane density, which is approximately $\propto e^{-R/R_D}$. What enters then is the dimensionless ratio of the average central column density to the threshold column density for H_2 , $A = \Sigma_{\text{gas}}(R=0)/\Sigma_{\text{thresh}}$.

Figure 10 shows the molecular fraction versus radius for one case where Σ_{ave} follows the observed HI column density (dashed lines) and another case where Σ_{ave} follows the inferred HI midplane density (solid lines). Blue curves assume $A = 10$ so the central region is highly molecular, and red curves assume $A = 2$. Both use $M = 4$ to get some breadth in the pdf. According to the discussion in Section 6.1, the deviation between the observed star formation rate and the dynamical rate, $\Sigma_{\text{gas}}/t_{\text{ff}}$, varies approximately exponentially with radius, and we interpreted this as a possible variation in the fraction of the ISM in the form of cold molecular clouds – molecular because this additional variation is not seen in the HI profiles, and cold because they are eventually involved with star formation, perhaps after 3D processes with self-gravity. Such a variation would be a straight line in Figure 10, and not a steeply falling curve. The falling curve means that the H_2 fraction has a sharp cutoff at some radius where the average column density of a cloud is comparable to the threshold column density in the local radiation field.

A second model with an H_2 cutoff is based on the theory in Krumholz et al. (2009a,b) which considers the molecular content of individual clouds in more detail. That model calculates the HI boundary layer of spherical clouds using H_2 self-absorption and dust absorption, and it uses this layer to determine the molecular fraction in the cloud given reasonable assumptions about the ratio of H_2 and HI densities. The model also assumes a constant ratio of radiation density to average gas density in order to maintain a 2-phase ISM.

In Krumholz et al. (2009b), the molecular fraction in a cloud approaches unity when their variable s greatly exceeds 1, where $s = \Sigma_{\text{comp}} Z / \psi$ for cloud column density Σ_{comp} in units of $M_\odot \text{pc}^{-2}$, Z is the metallicity in solar units, and ψ is a variable of order unity that depends on the ratio of radiation density to gas density. For their fiducial model with $Z \sim 1/8$ as for our galaxies, their equation (7) gives $\chi = 1.88$ for $\phi_{\text{CNM}} = 3$ and standard absorption and formation coefficients for H_2 , and their equation (10) then gives $\psi = 1.08$. Thus $s = 0.12 \Sigma_{\text{comp}}$. Now looking at their equation (39) for the quantity $R_{H_2} = n(H_2)/n(HI)$, and writing

$$\frac{n(H_2)}{n_{\text{total}}} = \frac{R_{H_2}}{1 + R_{H_2}} \quad (21)$$

we see that this molecular fraction approaches unity for $s \gg 11$, which corresponds in our case to $\Sigma_{\text{comp}} \gg 100 M_\odot \text{pc}^{-2}$. At $s \ll 8.4$, the molecular fraction goes to zero as $(s/12.1)^3$, which is $(\Sigma_{\text{comp}}/100)^3$. At low molecular fraction, this expression should be considered an upper limit. The result is a rapid drop in molecular fraction with the third power of the decreasing gas column density.

A similar rapid drop in molecular fraction is obtained from equation (2) in Krumholz et al. (2009a). We evaluate that equation again with metallicity $Z = 1/8$, which gives $\chi = 1.89$, $s = 151/\Sigma_{\text{comp}}$, $\delta \sim 0.21$ for large s , and molecular fraction approaching zero for low $\Sigma_{\text{comp}}/151$ as $(\Sigma_{\text{comp}}/129)^5$.

These rapid drops in molecular fraction for the pdf-threshold model and for the Krumholz et al. (2009b) and Krumholz et al. (2009a) models may explain the transition between the inner molecule-rich and outer molecule-poor regions of spiral galaxies, which seems to be relatively sharp in the observations by Bigiel et al. (2008) and others. Different processes seem to be at work for dIrr galaxies and perhaps also for the far-outer regions of spirals where the variations in SFR appear to be smoother. This is the primary reason for the diffuse cloud model in Section 6.2, which considers average H_2 formation and destruction rates in large volumes rather than threshold shielding in individual clouds.

7. Searching for the edges of star-forming disks

Dwarf irregulars probe star formation at extremely low surface densities, where 2D processes like spiral waves are inactive (Sect. 4) and the gas consumption time can exceed a Hubble time. In Figure 8 and Table 2, our sample is traced out to where the gas surface density is $\sim 1 M_\odot \text{pc}^{-2}$,

the stellar surface density is $\sim 0.1 M_{\odot} \text{ pc}^{-2}$, and the areal SFR is $\sim 10^{-5} M_{\odot} \text{ pc}^{-2} \text{ Myr}^{-1}$. Note that this SFR multiplied by the Hubble time equals the stellar surface density, so the observed rate is about equal to the average rate over the life of the galaxy.

These limits were also found in a previous study (Hunter et al. 2011) of four dIrr galaxies and a BCD galaxy using deep V and B band observations along with FUV from GALEX and HI from LITTLE THINGS (Hunter et al. 2012) and THINGS (Walter et al. 2008). We traced the disks down to about 29.5 mag arcsec $^{-2}$ in V band with $B-V \sim 0.3 - 0.4$, giving a mass-to-light ratio of 1.07 for a constant SFR with a Salpeter (1955) IMF (Bell & de Jong 2001). Then the stellar density is $\sim 0.06 M_{\odot} \text{ pc}^{-2}$ (0.03 for a Chabrier IMF). At the last traceable point of FUV or $H\alpha$, the gas surface density was $\sim 1 M_{\odot} \text{ pc}^{-2}$ and the star formation rate $\sim 10^{-5} M_{\odot} \text{ pc}^{-2} \text{ Myr}^{-1}$, as for the present sample. The gas surface density continued down to $0.1 M_{\odot} \text{ pc}^{-2}$ in DDO 53 and DDO 133, which are in the present sample too.

The same limits apparently apply to spiral galaxies. In M33, Grossi et al. (2011) found that star formation extends for about 10 inner scale lengths, to a radius of 60 arcmin where $\Sigma_{\text{HI}} \sim 1 M_{\odot} \text{ pc}^{-2}$ and $\Sigma_{\text{star}} \sim 0.1 M_{\odot} \text{ pc}^{-2}$. Both gas and stars go further than this although the stars have a shallower profile in the outer region. In NGC 7793 (Radburn-Smith et al. 2012), star formation ends before the gas and stars, at $\Sigma_{\text{gas}} \sim 1 M_{\odot} \text{ pc}^{-2}$, $\Sigma_{\text{star}} \sim 0.1 M_{\odot} \text{ pc}^{-2}$, and $\Sigma_{\text{SFR}} \sim 10^{-4.5} M_{\odot} \text{ pc}^{-2} \text{ Myr}^{-1}$. In NGC 2403 (Barker et al. 2012), star formation goes for 8 exponential scale lengths down to a V -band surface brightness of $\sim 29.5 \text{ mag arcsec}^{-2}$ and old stars continue further with a shallower slope, so this is about the same limit. In Hunter et al. (2013), NGC 801 and UGC 2885 have observed star formation to the same limits in Σ_{gas} , Σ_{star} , and σ_{SFR} .

Gas mass dominates stellar mass in these far outer regions, so the disk total gas pressure, scale height, and midplane density follow from the equations for a gaseous disk with a velocity dispersion σ_{gas} . When $\Sigma_{\text{gas}} = 1 M_{\odot} \text{ pc}^{-2}$, the pressure is $(\pi/2)G\Sigma_{\text{gas}}^2 = 34k_{\text{B}}$ for Boltzmann constant k_{B} , the scale height is $\sigma_{\text{gas}}^2/\pi G\Sigma_{\text{gas}} = 4.7 \text{ kpc}$, and the midplane mass density is $0.5\pi G(\Sigma_{\text{gas}}/\sigma_{\text{gas}})^2 = 7.22 \times 10^{-27} \text{ g cm}^{-3}$, which corresponds to $n(\text{HI}) = 0.0033 \text{ cm}^{-3}$. Here we have assumed a gaseous velocity dispersion $\sigma_{\text{gas}} = 8 \text{ km s}^{-1}$ for the far outer parts from Table 2. Also from these numbers, $\tau_{\text{ff}} = 780 \text{ Myr}$. If $\Sigma_{\text{SFR}} = \epsilon\Sigma_{\text{gas}}/\tau_{\text{ff}}$, then $\epsilon = 7.8 \times 10^{-3}$ when $\Sigma_{\text{SFR}} = 10^{-5} M_{\odot} \text{ pc}^{-2} \text{ Myr}^{-1}$. This value of ϵ is consistent with the values found at large radii in the lower right panel of Figure 6.

Stars and HI gas continue further than star formation in most of the galaxies mentioned above, and they do so for many in the present sample as well. The radial profiles in Figure 8 are plotted only out to the edge of the FUV light where the SFR can be measured. Figure 11 plots the HI and derived data out as far as the observations go. The 3D density is determined from Σ_{gas} assuming that gas dominates stars, as above, and using the observed velocity dispersion at the appropriate radius. The free fall time comes from the density. In some cases, the full HI radial profiles go out nearly twice as far as the star forming parts shown in Figure 8, and the slopes change in the outer parts. One of the red lines in each panel is the slope tabulated in Table 2, which is from the radial range where FUV is detected, while another red line suggests a different slope, more appropriate

to the outer regions.

The smooth exponential profiles and large τ_{ff} for the outer regions shown in Figure 11 call into question some of the modern ideas about cosmic accretion. Cosmic accretion seems required to explain the continuous presence of star formation in galaxies of moderate to low mass when the gas consumption time is only ~ 0.2 times the current Hubble time (Dekel et al. 2013). For $\sim 2\%$ efficiency, the consumption time is $50\tau_{\text{ff}}$. This replenishment scenario applies mostly to the inner parts of spirals. However, when the consumption time is comparable to or longer than the Hubble time, accretion is not needed for the same reason, and may even result in too much gas collecting in the outer parts. In Figure 11, the HI profiles do not show an excess when τ_{ff} gets large, they continue to decline with about the V-band scale length in most cases (which is even steeper than for the inner regions). Three galaxies in the upper left panel have more slowly declining Σ_{gas} and $n(\text{HI})$; these are DDO 75 (Sextans A), DDO 154 (NGC 4789A), and Haro 29.

As mentioned above, stellar disks often continue further out than the known star formation, in which case the disks cannot be made there but have to move there. Outer disks also have smooth exponential surface density profiles like inner disks. Bars (Debattista et al. 2006) and spiral waves (Berrier & Sellwood 2014) could be responsible for the exponential profiles in the main disks of spiral galaxies and barred dIrr galaxies, and these structures might even scatter stars to the far outer regions where star formation stops (Roškar et al. 2008). However, in non-barred dIrr galaxies, the only irregular structures that seem capable of scattering stars are gas clumps, which might also make exponentials (Elmegreen & Struck 2013).

Our observation that star formation follows the dynamical time at the midplane density implies that 3D self-gravity in the gas is still important even without spirals. This 3D gravity should make dense clouds throughout the disks in our sample. Moreover, the dominance of gas in the outer parts (the midplane gas-to-star density ratio is ~ 10 according to Table 2) implies that such clouds are the main scattering sites for ambient stars. Thus the outer disk profiles of old stars could be the result of stellar scattering off of massive conglomerations of diffuse clouds.

8. Conclusions

The star formation properties of 20 dIrr galaxies have been examined in relation to the average radial profiles of gas and stellar mass, FUV intensity, velocity dispersion, and rotation rate. The disks are found to be relatively thick and stable against 2D self-gravitational processes, which probably explains why there are no spiral waves, but which also suggests that star formation is fundamentally a 3D process. The star formation rate agrees fairly well with the conventional expression, $\epsilon_{\text{ff}}\Sigma_{\text{gas}}/\tau_{\text{ff}}$, also giving the usual efficiency, ϵ_{ff} , of one per cent, when the free fall time, τ_{ff} , uses the 3D midplane density evaluated from the HI column density divided by twice the HI scale height. The resulting correlation is fairly tight and the same for all galaxies, suggesting that ambient self-gravity in 3D is important for regulating the SFR. We find a radial variation in ϵ_{ff}

that has an exponential form with a scale length equal to about twice the V-band scale length. The origin of this ϵ_{ff} variation is not obvious as it is likely to come from a combination of effects including radial variations in the molecular fraction and in the fraction of the gas that is cold and dense enough to collapse into stars. A simple model considering only the molecular fraction in a diffuse interstellar medium from a balance between H_2 formation at the rms density and H_2 destruction at the mean density and radiation field, gets about the observed trend when the atomic and molecular layer thicknesses increase with radius in the same way.

Another model using the radial profile of FUV radiation to determine the trend in molecular fraction gives the observed SFR profile too, but only when the molecular layer does not flare like the HI layer. This seems to be a reasonable proposition that might be tested in edge-on dIrr galaxies. In this second model, the SFR is proportional to the ratio of the molecular surface density to the molecular dynamical time with a constant efficiency. In the absence of a molecular flare, this ratio is the same as the 1.5 power of the molecular surface density. This scaling with molecules is different from that in the inner parts of spiral galaxies where the SFR seems to scale with the 1st power of the molecular density (see references in Section 1), but there are other differences between these two regions also, such as the lack of a gaseous flare, a closer correspondence between H_2 and the more easily observed CO, and a higher density, opacity and degree of self-gravity for the inner regions of spirals.

Other models that consider a threshold for the presence of H_2 in clouds, as might arise from a shielding layer around the molecular part of a massive cloud, imply sharp declines in the radial profiles of the molecular fraction that are not inferred from the smooth profiles of everything else observed here. Perhaps these threshold models explain the difference between the inner and outer disk properties in spiral galaxy, but they do not appear to apply to dIrr disks alone.

The radial profiles of the gas surface densities are generally shallower than the radial profiles of the V-band light, which are shallower still than the radial profiles of the FUV light. All have approximately exponential shapes, and the scale lengths center around factors of 2, 1, and 2/3, respectively, times the V-band scale length, R_{D} . The radial profiles of the gaseous and stellar scale heights are exponential also, and similar to each other with a scale length of twice R_{D} . As a result, the midplane densities for stars and gas have different profiles than the projected densities. For example, volume emissivities for V and FUV bands drop faster than their surface brightnesses, and the radiation fields in these bands, given approximately by the volume emissivity divided by the opacity, drop slower than the surface brightnesses. Radiation fields are stronger in the outer parts of galaxies than the surface brightness profiles suggest.

The conditions in our galaxies could be representative of the conditions in the far-outer parts of spiral galaxies, where gas also tends to dominate stars and thickness effects become important for stabilization. Spiral galaxies still have spiral waves in the outer parts, however, while dIrrs do not, so there could be a difference in how GMCs are assembled in the two cases.

REFERENCES

- Ashley, T., Simpson, C.E., & Elmegreen, B.G. 2013, *AJ*, 146, 42
- Barker, M. K., Ferguson, A. M. N., Irwin, M. J., Arimoto, N., & Jablonka, P. 2012, *MNRAS*, 419, 1489
- Barnes, K. L., van Zee, L., Côté, S., & Schade, D. 2012, *ApJ*, 757, 64
- Barriault, L., Joncas, G., Falgarone, E. et al. 2010, *MNRAS*, 406, 2713
- Bell, E. F., & de Jong, R. S. 2001, *ApJ*, 550, 212
- Banerjee, A., Jog, C.J., Brinks, E., & Bagetakos, I. 2011, *MNRAS*, 415, 687
- Berrier, J.C., & Sellwood, J. A. 2014, arXiv1412.0979
- Bigiel, F., Leroy, A., Walter, F., Brinks, E., de Blok, W. J. G., Madore, B., & Thornley, M. D. 2008, *AJ*, 136, 2846
- Bigiel, F., Leroy, A., Walter, F., Blitz, L., Brinks, E., de Blok, W.J.G., Madore, B. 2010, *AJ*, 140, 1194
- Boissier, S., Prantzos, N., Boselli, A., Gavazzi, G. 2003, *MNRAS*, 346, 1215
- Bolatto, A.D., Leroy, A.K., Jameson, K., et al. 2011, *ApJ*, 741, 12
- Bolatto, A.D., Wolfire, M., Leroy, A.K. 2013, *ARA&A*, 51, 207
- Cardelli, J. A., Clayton, G. C., & Mathis, J. S. 1989, *ApJ*, 345, 245
- Dalcanton, J.J., Yoachim, P., & Bernstein, R.A. 2004, *ApJ*, 608, 189
- Debattista V. P., Mayer L., Carollo C. M., Moore B., Wadsley J., & Quinn T., 2006, *ApJ*, 645, 209
- Dekel, A., Zolotov, A., Tweed, D., et al. 2013, *MNRAS*, 435, 999
- Dib, S., Bell, E. & Burkert, A. 2006, *ApJ*, 638, 797
- Dobbs, C.L., Krumholz, M.R., Ballesteros-Paredes, J., Bolatto, A.D., Fukui, Y., Heyer, M., Mac Low, M.-M., Ostriker, E.C., Vázquez-Semadeni, E. 2013, in *Protostars and Planets VI*, University of Arizona Press, eds. H. Beuther, R. Klessen, C. Dullemond, Th. Henning, arXiv:1312.3223
- Elmegreen B. G., 1993, *ApJ*, 411, 170
- Elmegreen, B.G. 2002, *ApJ*, 577, 206
- Elmegreen, B.G. 2011, *ApJ*, 737, 10

- Elmegreen B. G., 2013, in Wong T., Ott J., eds, Proc. IAU Symp. Vol. 292, Molecular Gas, Dust, and Star Formation. Cambridge Univ. Press, Cambridge, p. 35
- Elmegreen, B.G., Rubio, M., Hunter, D.A., Verdugo, C., Brinks, E., & Schrupa, A. Nature, 495, 487
- Elmegreen, B.G., & Struck, C., 2013, ApJ, 775, L35
- Evans, N.J., II., Heiderman, A., & Vutisalchavakul, N. 2014, ApJ, 782, 114
- Fazio, G. G., Hora, J. L., & Allen, L. E. et al. 2004, ApJS, 154, 10
- Federman, S. R., Glassgold, A. E., Jenkins, E. B., & Shaya, E. J. 1980, ApJ, 242, 545
- Feldmann, R. 2013, MNRAS, 433, 1910
- Ferguson, A. M. N., Wyse, R. F. G., Gallagher, J. S., & Hunter, D. A. 1998, AJ, 111, 2265
- Gil de Paz, A., et al. 2005, ApJ, 627, L29
- Grossi, M., Hwang, N., Corbelli, E., Giovanardi, C., Okamoto, S., & Arimoto, N. 2011, A&A, 533, A91
- Hodge, P. W., & Hitchcock, J. L. 1966, PASP, 78, 79
- Hollenbach, D.J., Werner, M.W., & Salpeter, E.E. 1971, ApJ, 163, 165
- Hunt, L. K., Thuan, T. X., Izotov, Y. I., & Sauvage, M., 2010, ApJ, 712, 164
- Hunter, D. A., & Plummer, J. D. 1996, ApJ, 462, 732
- Hunter, D.A., Elmegreen, B.G., & Baker, A.L. 1998, ApJ, 493, 595
- Hunter, D. A. & Elmegreen, B. G. 2006, ApJ, 162, 49
- Hunter, D. A., Elmegreen, B. G., & Ludka, B. C. 2010, AJ, 139, 447
- Hunter, D.A., Elmegreen, B.G., Oh, S.-H., Anderson, E., Nordgren, T.E., Massey, P., Wilsey, N., & Riabokin, M., 2011, AJ, 142, 121
- Hunter, D.A., Ficut-Vicas, D., Ashley, T., et al. 2012, AJ, 144, 134
- Hunter, D.A., Elmegreen, B.G., Rubin, V.C., Ashburn, A., Wright, T., Józsa, G.I.G., Struve, C., 2013, AJ, 146, 92
- Johnson, M. C., Hunter, D. A., Oh, S.-H., et al. 2012, AJ, 144, 152
- Johnson, M. et al. 2015, submitted to AJ
- Jura, M. 1975, ApJ, 197, 581

- Kennicutt, R. C., Jr. 1989, *ApJ*, 344, 685
- Kennicutt, R.C., Jr. 1998, *ApJ*, 498, 541
- Kennicutt, R.C., Jr., Calzetti, D., Walter, F., et al. 2007, *ApJ*, 671, 333
- Kennicutt, R.C., & Evans, N.J. 1 2012, *ARA&A*, 50, 531
- Kim, C.-G., Ostriker, E.C., & Kim, W.-T. 2013, *ApJ*, 776, 1
- Kobulnicky, H. A., & Skillman, E. D. 1996, *ApJ*, 471, 211
- Kobulnicky, H. A., & Skillman, E. D. 1997, *ApJ*, 489, 636
- Kraljic, K., Renaud, F., Bournaud, F., Combes, F., Elmegreen, B., Emsellem, E., Teyssier, R. 2014, *ApJ*, 784, 112
- Krumholz, M.R., & Tan, J.C. 2007, *ApJ*, 654, 304
- Krumholz, M. R., McKee, C. F., & Tumlinson, J. 2009, *ApJ*, 699, 850
- Krumholz, M.R., McKee, C.F., & Tumlinson, J. 2009, *ApJ*, 693, 216
- Krumholz, M.R., Leroy, A.K., McKee, C.F. 2011, *ApJ*, 731, 25
- Krumholz, M.R., Dekel, A., & McKee, C.F. 2012, *ApJ*, 745, 69
- Krumholz, M.R. 2013, *MNRAS*, 436, 2747
- Lada, C.J., Lombardi, M., & Alves, J.F. 2010, *ApJ*, 724, 687
- Lada, C.J., Lombardi, M., Roman-Zuniga, C., Forbrich, J., & Alves, J.F. 2013, *ApJ*, 778, 133
- Lee, M.-Y., Stanimirovic, S., Douglas, K.A., et al. 2012, *ApJ*, 748, 75
- LeLièvre, M., & Roy, J.-R. 2000, *AJ*, 120, 1306
- Leroy, A.K., Walter, F., Brinks, E., Bigiel, F., de Blok, W. J. G., Madore, B., & Thornley, M. D. 2008, *AJ*, 136, 2782
- Liu, G., Koda, J., Calzetti, D., Fukuhara, M., Momose, R. 2011, *ApJ*, 735, 63
- Lombardi, M., Lada, C. J., & Alves, J. 2010, *A&A*, 512A, 67
- Mac Low, M.M., & Glover, S.C.O. 2012, *ApJ*, 746, 135
- Martin, D. C., Fanson, J., & Schiminovich, D. et al. 2005, *ApJ*, 619, 1
- McKee, C.F., & Krumholz, M.R. 2010, *ApJ*, 709, 308

- Meurer, G. R., Carignan, C., Beaulieu, S. F., & Freeman, K. C. 1996, *AJ*, 111, 1551
- Momose, R., Koda, J., Kennicutt, R.C., Jr., Egusa, F., Calzetti, D., Liu, G., Meyer, J.D., Okumura, S.K., Scoville, N.Z., Sawada, T., & Kuno, N. 2013, *ApJL*, 772, L13
- Narayan, C.A., & Jog, C.J. 2002, *A&A*, 394, 89
- Nordlund, Å., & Padoan, P. 1999, in *Interstellar Turbulence*, ed. J. Franco & A. Carramiñana (Cambridge: Cambridge Univ. Press), 218
- Oh, S-H., Hunter, D.A., Brinks, E., et al. 2015, *AJ*, in press.
- Ostriker, E.C., McKee, C.F., & Leroy, A.K. 2010, *ApJ*, 721, 975
- Padoan P., Nordlund A., Jones B. J. T., 1997, *MNRAS*, 288, 145
- Pagel, B. E. J., Edmunds, M. G., & Smith, G. 1980, *MNRAS*, 193, 219
- Pineda, J. E., Caselli, P., & Goodman, A. A. 2008, *ApJ*, 679, 481
- Radburn-Smith, D.J., Roškar, R., Debattista, V.P., Dalcanton, J.J., Streich, D., de Jong, R.S., Vlajić, M., Holwerda, B.W., Purcell, C.W., Dolphin, A.E., & Zucker, Daniel B. 2012, *ApJ*, 753, 138
- Rafikov, R.R. 2001, *MNRAS*, 323, 445
- Rahman, N., Bolatto, A.D., Wong, T., Leroy, A.K. 2011, *ApJ*, 730, 72
- Romeo, A.B. 1992, *MNRAS*, 256, 307
- Romeo, A.B., & Wiegert, J. 2011, *MNRAS*, 416, 1191
- Roškar, R., Debattista, V. P., Quinn, T. R., Stinson, G. S., & Wadsley, J. 2008, *ApJ*, 684, L79
- Roy, J.-R., Belley, J., Dutil, Y., & Martin, P. 1996, *ApJ*, 460, 284
- Safronov, V. S. 1960, *Ann.Ap.*, 23, 979
- Schruba, A., Leroy, A. K., Walter, F., et al. 2011, *AJ*, 142, 37
- Shetty R., Kelly B. C., & Bigiel F., 2013, *MNRAS*, 430, 288
- Shetty, R., Clark, P.C., & Klessen, R.S. 2014, *MNRAS*, 442, 2208
- Shi, Y., Helou, G., Yan, L., Armus, L., Wu, Y., Papovich, C., Stierwalt, S. 2011, *ApJ*, 733, 87
- Shi, Y., Armus, L., Helou, G., Stierwalt, S., Gao, Y., Wang, J., Zhang, Z.-Y., Gu, Q. 2014, *Nature*, 514, 335
- Spitzer, L., Jr., & Jenkins, E. B. 1975, *ARA&A*, 13, 133

- Staveley-Smith, L., Davies, R. D., & Kinman, T. D. 1992, MNRAS, 258, 334
- Sternberg, A., Le Petit, F., Roueff, E., Le Bourlot, J. 2014, ApJ, 790, 10
- Swaters, R. A. 1999, Ph. D. Thesis, University of Groningen
- Thilker, D.A. et al. 2005, ApJ, 619, L79
- Toomre, A. 1964, ApJ, 139, 1217
- van den Bergh, S. 1988, PASP, 100, 344
- van der Kruit, P. C., & Freeman, K. C. 2011, ARA&A, 49, 301
- van Zee, L., Haynes, M. P., Salzer, J. J., & Broeils, A. H. 1997, AJ, 113, 1618
- Walter, F., Brinks, E., de Blok, W. J. G., Bigiel, F., Kennicutt, R. C., Jr., Thornley, M. D., & Leroy, A. 2008, AJ, 136, 2563
- Wang, B., & Silk, J. 1994, ApJ, 427, 759
- Werner, M. W., Roellig, T. L., & Low, F. J. et al. 2004, ApJS, 154, 1
- Westfall, K.B., Andersen, D.R., Bershady, M.A., Martinsson, T.P.K., Swaters, R.A., & Verheijen, M.A.W. 2014, ApJ, 785, 43
- Wong, T., & Blitz, L. 2002, ApJ, 569, 157
- Vandervoort, P.O. 1970, ApJ, 161, 87
- Yang, C.-C., Gruendl, R.A., Chu, Y.-H., Mac Low, M.-M., Fukui, Y., 2007, ApJ, 671, 374
- Yim, K., Wong, T., Xue, R., Rand, R.J., Rosolowsky, E., van der Hulst, J.M., Benjamin, R., & Murphy, E.J. 2014, AJ, 148, 127
- Zhang, H.-X., Hunter, D.A., Elmegreen, Bruce G., Gao, Y., & Schrupa, A. 2012, AJ, 143, 47

Table 1. The Galaxy Sample

Galaxy	D (Mpc)	M_V (mag)	R_D^a (kpc)	$\log \text{SFR}_D^{FUVb}$ ($M_\odot \text{ yr}^{-1} \text{ kpc}^{-2}$)
CVnIdwA	3.6	-12.4	0.57 ± 0.12	-2.48 ± 0.01
DDO 101	6.4	-15.0	0.94 ± 0.03	-2.81 ± 0.01
DDO 126	4.9	-14.9	0.87 ± 0.03	-2.10 ± 0.01
DDO 133	3.5	-14.8	1.24 ± 0.09	-2.62 ± 0.01
DDO 154	3.7	-14.2	0.59 ± 0.03	-1.93 ± 0.01
DDO 168	4.3	-15.7	0.82 ± 0.01	-2.04 ± 0.01
DDO 210	0.9	-10.9	0.17 ± 0.01	-2.71 ± 0.06
DDO 216	1.1	-13.7	0.54 ± 0.01	-3.21 ± 0.01
DDO 50	3.4	-16.6	1.10 ± 0.05	-1.55 ± 0.01
DDO 52	10.3	-15.4	1.30 ± 0.13	-2.43 ± 0.01
DDO 53	3.6	-13.8	0.72 ± 0.06	-2.41 ± 0.01
DDO 70	1.3	-14.1	0.48 ± 0.01	-2.16 ± 0.00
DDO 75	1.3	-13.9	0.22 ± 0.01	-1.07 ± 0.01
DDO 87	7.7	-15.0	1.31 ± 0.12	-1.00 ± 0.01
Haro 29	5.8	-14.6	0.29 ± 0.01	-1.07 ± 0.01
IC 1613	0.7	-14.6	0.58 ± 0.02	-1.99 ± 0.01
NGC 2366	3.4	-16.8	1.36 ± 0.04	-1.66 ± 0.01
NGC 3738	4.9	-17.1	0.78 ± 0.01	-1.53 ± 0.01
UGC 8508	2.6	-13.6	0.27 ± 0.01	...
WLM	1.0	-14.4	0.57 ± 0.03	-2.05 ± 0.01

^a R_D is the disk scale length measured from V -band images. From Hunter & Elmegreen (2006).

^b SFR_D^{FUV} is the SFR determined from *GALEX* FUV fluxes (Hunter et al. 2010), with an update of the *GALEX* FUV photometry to the GR4/GR5 pipeline reduction presented in Zhang et al. (2012).

Table 2. Radial Trends

V^a	$\ln V(0)$	$V(0) - V(4R/R_D)$	Slope
Σ_{gas}	2.28 ± 0.69	$9.77 - 1.589 M_{\odot} \text{ pc}^{-2}$	-0.45 ± 0.32
Σ_{star}	1.58 ± 1.26	$4.87 - 0.134 M_{\odot} \text{ pc}^{-2}$	-0.90 ± 0.36
n_{gas}	-0.83 ± 0.91	$0.44 - 0.0116 \text{ cm}^{-3}$	-0.91 ± 0.54
n_{star}	-1.23 ± 1.52	$0.29 - 0.0011 \text{ cm}^{-3}$	-1.40 ± 0.49
σ_{gas}	2.47 ± 0.34	$11.8 - 8.0 \text{ km s}^{-1}$	-0.10 ± 0.10
H_{gas}	48.42 ± 0.59	$0.35 - 2.13 \text{ kpc}$	0.45 ± 0.28
H_{star}	48.12 ± 0.71	$0.26 - 1.88 \text{ kpc}$	0.50 ± 0.25
$n_{\text{star}}/n_{\text{gas}}$	-0.40 ± 1.26	$0.67 - 0.0954$	-0.49 ± 0.51
$\Sigma_{\text{gas}}/\tau_{\text{ff}}$	-1.94 ± 1.08	$0.144 - 0.0038 M_{\odot} \text{ pc}^{-2} \text{ Myr}^{-1}$	-0.91 ± 0.58
Σ_{SFR}	-5.75 ± 1.25	$0.0032 - 1.03 \times 10^{-5} M_{\odot} \text{ pc}^{-2} \text{ Myr}^{-1}$	-1.43 ± 0.58
τ_{ff}	35.30 ± 34.43	$0.068 - 0.42 \text{ Gyr}$	0.45 ± 0.27

^a V represents the “variable” given in the first column; the second column is the natural log of this variable in the galaxy center, the 3rd column is the range out to 4 scale lengths, and the 4th column is the slope on a ln-linear plot. The exponential V-band light profile would have a slope of -1 .

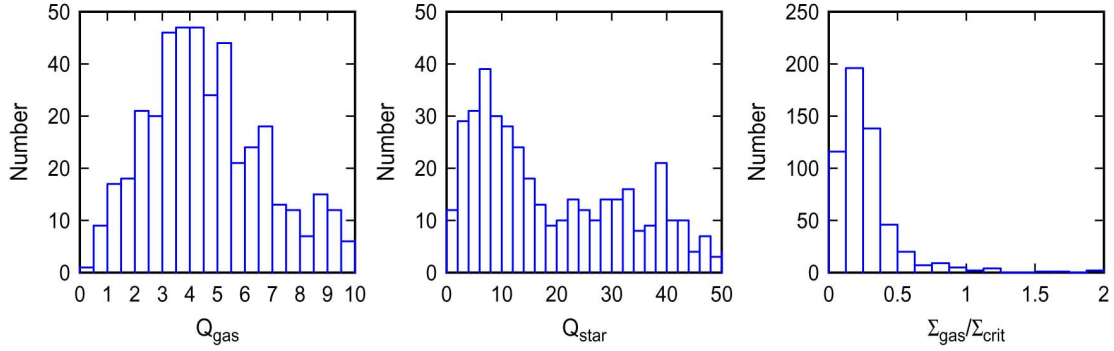


Fig. 1.— (left and center) The distribution of gaseous and stellar Q values for all of the radii and galaxies in our survey. (right) The distribution of the ratio of the local HI surface density and the Kennicutt (1989) critical density for star formation, based on the 2D stability analysis. The dIrr galaxies considered here have high values of Q_{gas} and very high values of Q_{star} , making them effectively stable against radial motions and spiral waves driven by self-gravity. The low values of $\Sigma_{\text{gas}}/\Sigma_{\text{crit}}$ suggest the same thing.

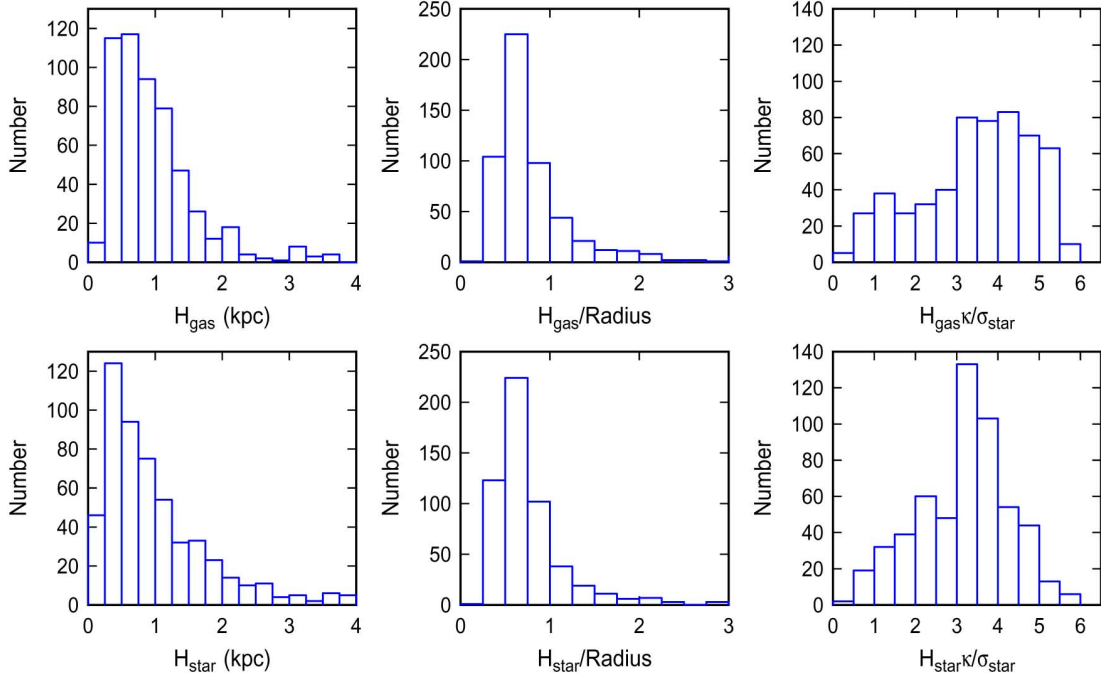


Fig. 2.— The distributions of vertical scale heights for gas (top) and stars (bottom) for all of the radii and galaxies in our survey. The scale height is given in three forms: absolute (left), relative to the local radius (center), and relative to the local epicyclic scale (right). By all measures, the scale heights are large, which weakens self-gravitational forces parallel to the disks and makes the 2D gravitational instability even less effective than indicated by the large Q values alone.

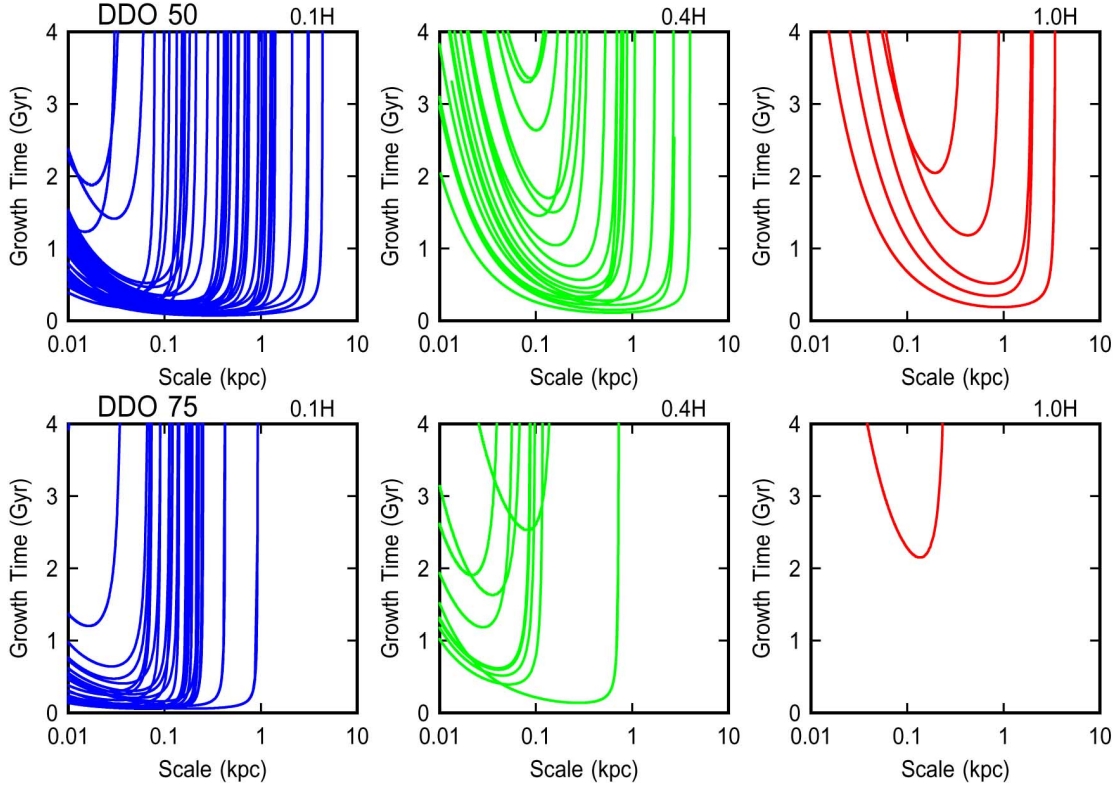


Fig. 3.— Dispersion relations for the 2D, two-fluid gravitational instability, plotted as unstable growth time versus perturbation scale, with one curve for each radial interval in galaxies DDO 50 (top) and DDO 75 (bottom). Thickness effects are included in a self-consistent way for the right-hand panels, but for the left-hand and center panels, thicknesses equal to 0.1 and 0.4 times the true thicknesses are assumed just to show the functional forms of these relationships. When the thickness is forced to be smaller than the true thickness, the gravitational instability is stronger and the growth time is smaller. These left and center panels are unrealistic, however. At the full galaxy thickness, the growth time of the 2D two-fluid instability is very long, indicating relatively weak self-gravity compared to other forces.

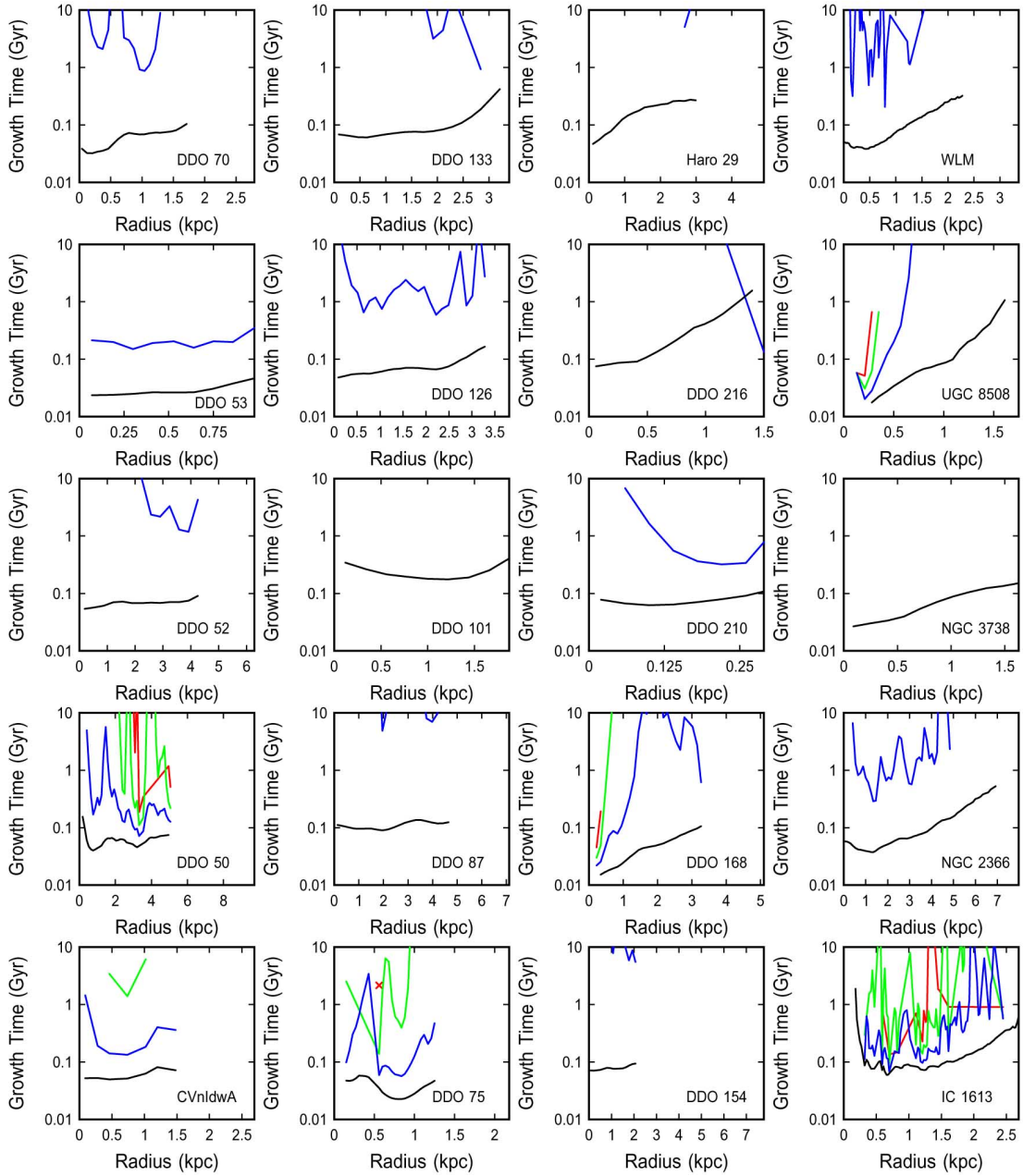


Fig. 4.— The fastest growth times regardless of perturbation scale for the 2D two-fluid instability are shown versus radius for all of the galaxies in our survey. The black curves assume zero thickness to maximize the self-gravity of the disk. Even then, the growth times are long in some cases, equal to or exceeding 100 Myr. The blue curves assume disk thicknesses equal to 0.1 times the true thickness, while green and red curves assume 0.4 and 1 times the true thickness. Very few galaxies have unstable growth times less than 10 Gyr at the full thickness, so there are almost no red curves here.

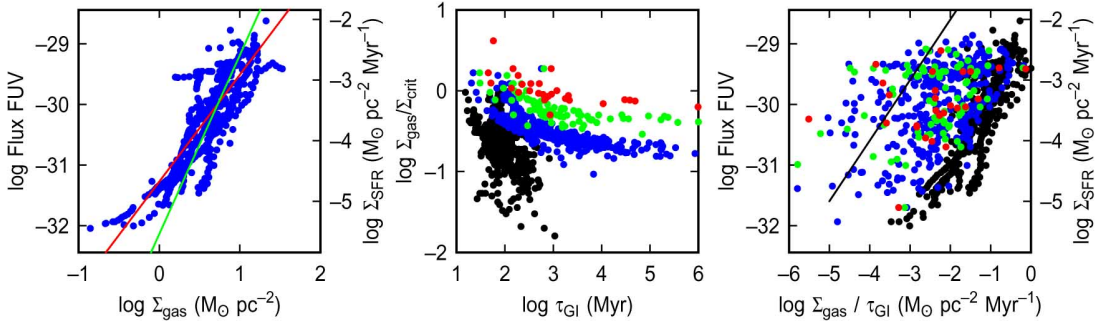


Fig. 5.— (left) The extinction-corrected FUV flux density in units of $\text{erg cm}^{-2} \text{ s}^{-1} \text{ Hz}^{-1} \text{ arcsec}^{-1}$, plotted on a \log_{10} scale, is shown versus the \log_{10} of the gas surface density, as determined from HI with a correction for He and heavy elements, for all radial annuli and galaxies in our survey. The red line is a fit to all of the points (slope = 1.76 ± 0.08) and the green line is an average of the fits to each galaxy (slope = 2.95 ± 2.09). The areal SFR is on the right-hand axis. (center) The ratio of the gas surface density to the critical value from Kennicutt (1989) is plotted versus the fastest growth time of the 2D two-fluid instability for the four cases of disk thickness indicated by color (cf. Fig. 3 and 4). The red points are the most realistic because they use the full thickness of the galaxy to determine the self-gravitational forces. Sub-threshold surface densities have long growth times, too long to control star formation (i.e., they are a Gyr or more when the full disk thickness is considered). (right) The FUV flux and areal SFR increases with the ratio of the gas surface density to the 2D gravitational instability time, but there is too much scatter for all but the artificial zero-thickness case (black points) to conclude that the 2D instability controls star formation. The black line has a slope of 1 with arbitrary height.

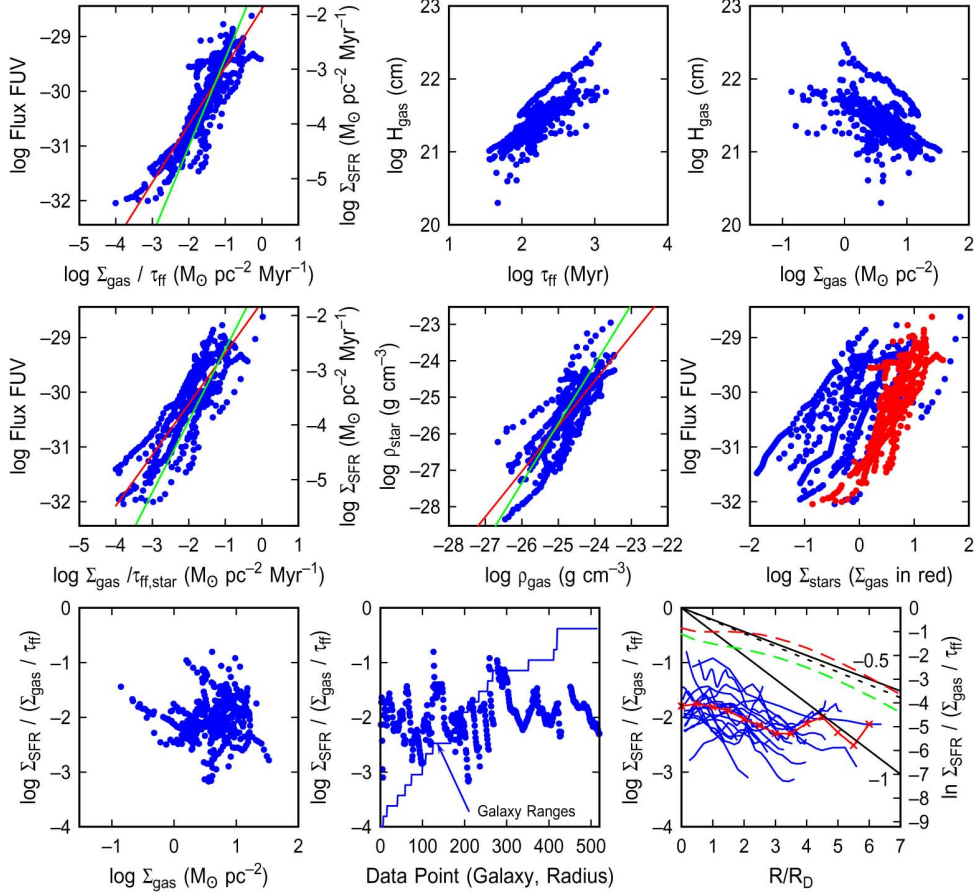


Fig. 6.— Correlations suggesting that the areal SFR equals an efficiency ϵ_{ff} of $\sim 1.0\%$ (lower left) of the HI gas surface density per unit free-fall time at the midplane HI density, with a radial dependence of ϵ_{ff} (lower right) that parallels the dependence of the molecular fraction in a diffuse interstellar medium (green dashed curve). Top and middle left: SFR versus model rates using the gas and stellar midplane densities, respectively. The correlations are similar because the stellar density is proportional to the gas density (central panel, middle row), but it is tighter using the gas rate (top left panel and right-hand panel in the middle row). The quadratic relation between the SFR and the gas surface density (Fig. 5) corresponds to the upper left panel because of the dependence of the gas scale height on the free fall time and surface density (upper center and right panels). In the central panel of the bottom row, ϵ_{ff} is plotted versus radius for all of the galaxies from left to right, as indicated by each horizontal segment in the rising curve. A radial decrease is evident for each one, as also shown in the lower right panel where each galaxy is a different curve with an average slope given by the dotted black line. The other two lines in the lower right have fiducial slopes of -0.5 and -1 for comparison. The red dashed curve is the molecular fraction when the radial profile of FUV light is used to determine the dissociation rate. This red-dash curve is not a good fit to the data in these cases where it is assumed that the H_2 and HI thicknesses increase with radius in the same way. The FUV model is a better fit if the H_2 thickness is constant, as discussed in Sect. 6.4.

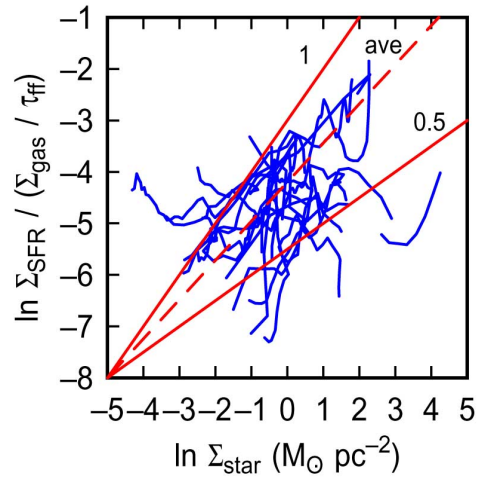


Fig. 7.— Star formation efficiency versus the stellar mass surface density, with natural logs.

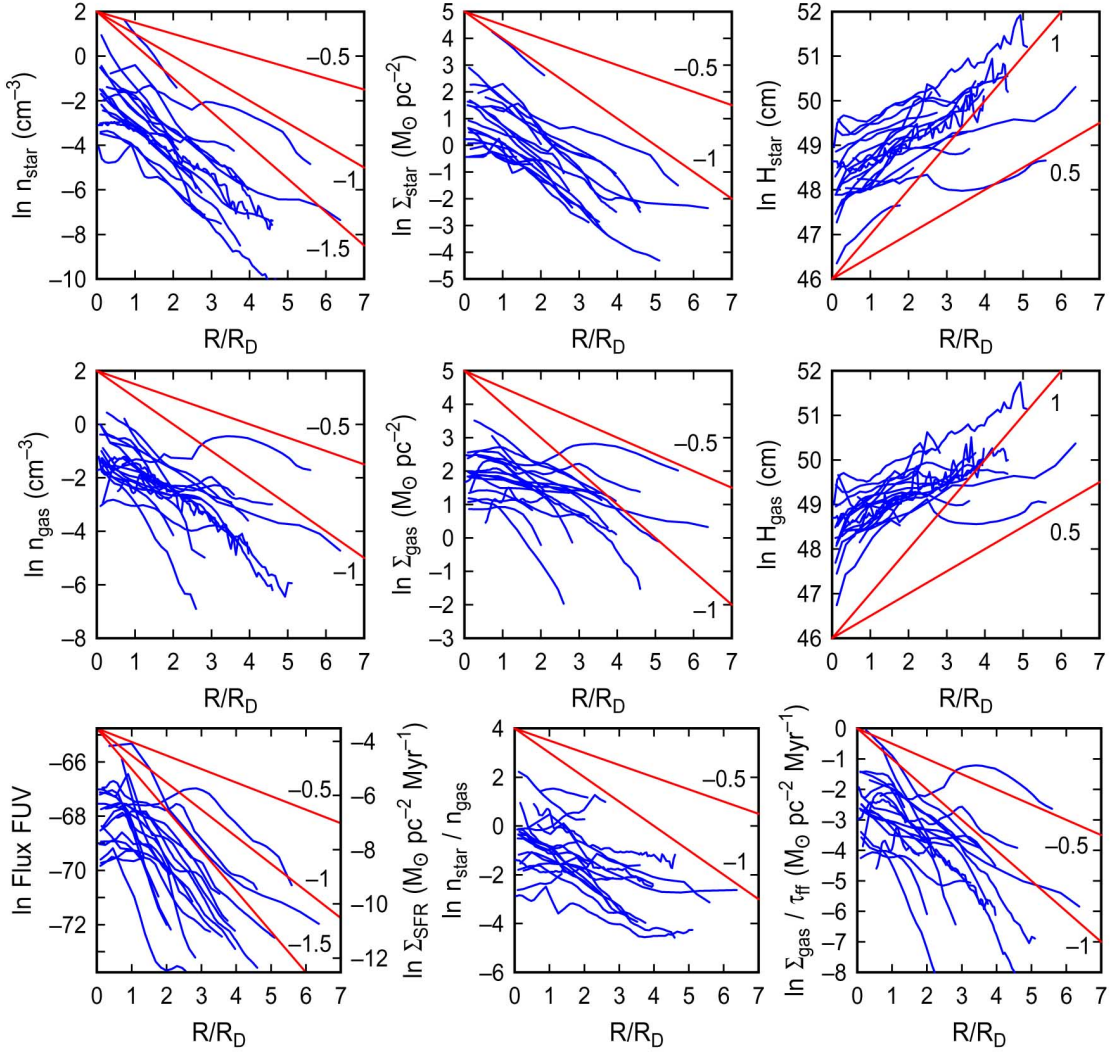


Fig. 8.— Radial profiles of various quantities plotted with natural log on the ordinate to facilitate comparisons with the exponential disk profile. The straight lines have slopes in increments of 0.5.

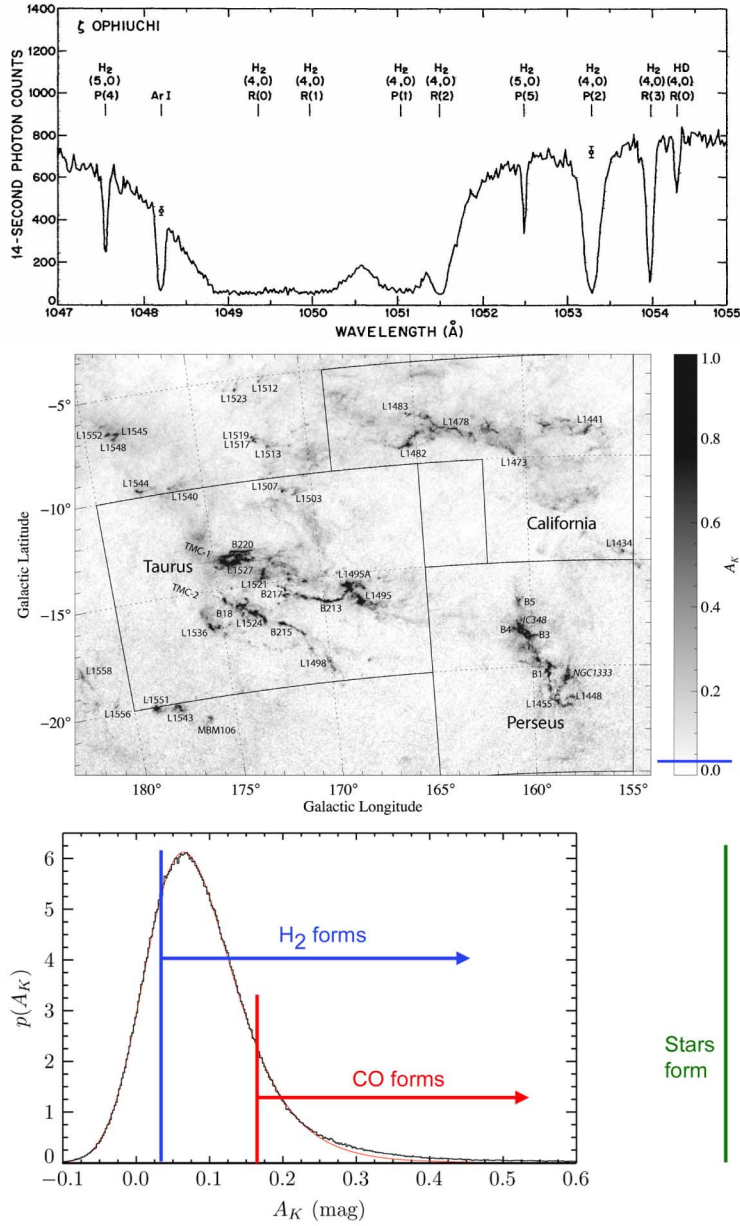


Fig. 9.— (top) Spectrum of molecular hydrogen absorption on the line of sight to ζ Oph showing nearly complete absorption from a standard-size diffuse cloud. (middle) The Perseus and Taurus regions studied by Lombardi et al. (2010) with the threshold extinction for H₂ formation indicated by a horizontal bar on the gray-scale calibration. Most of the field of view has an extinction exceeding the threshold. (bottom) Distribution function for column density in the Perseus-Taurus region, from Lombardi et al. (2010) showing the H₂, CO, and star formation thresholds discussed in the text. A large fraction of the diffuse interstellar medium in the solar neighborhood is H₂.

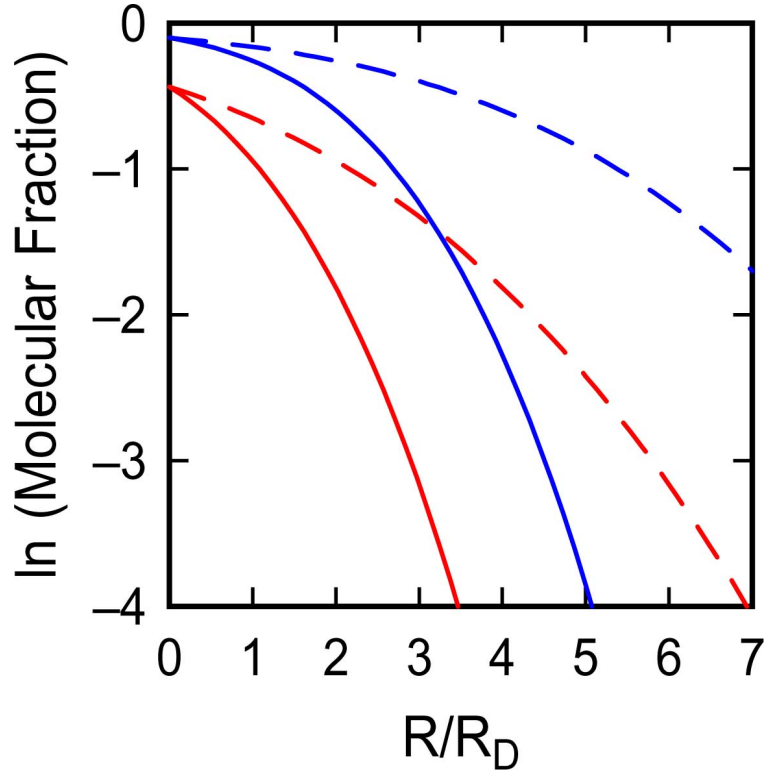


Fig. 10.— Radial profiles of molecular fraction in two threshold models for H_2 formation. Blue curves are for a highly molecular ISM in the center, where the ratio of the mean surface density of gas to the H_2 formation threshold equals 10, and red curves are for a moderate molecular fraction in the center, where this ratio equals 2. Dashed curves assume the average cloud column density scales with the total HI surface density and solid curves assume the average cloud column density scales with the midplane 3D density.

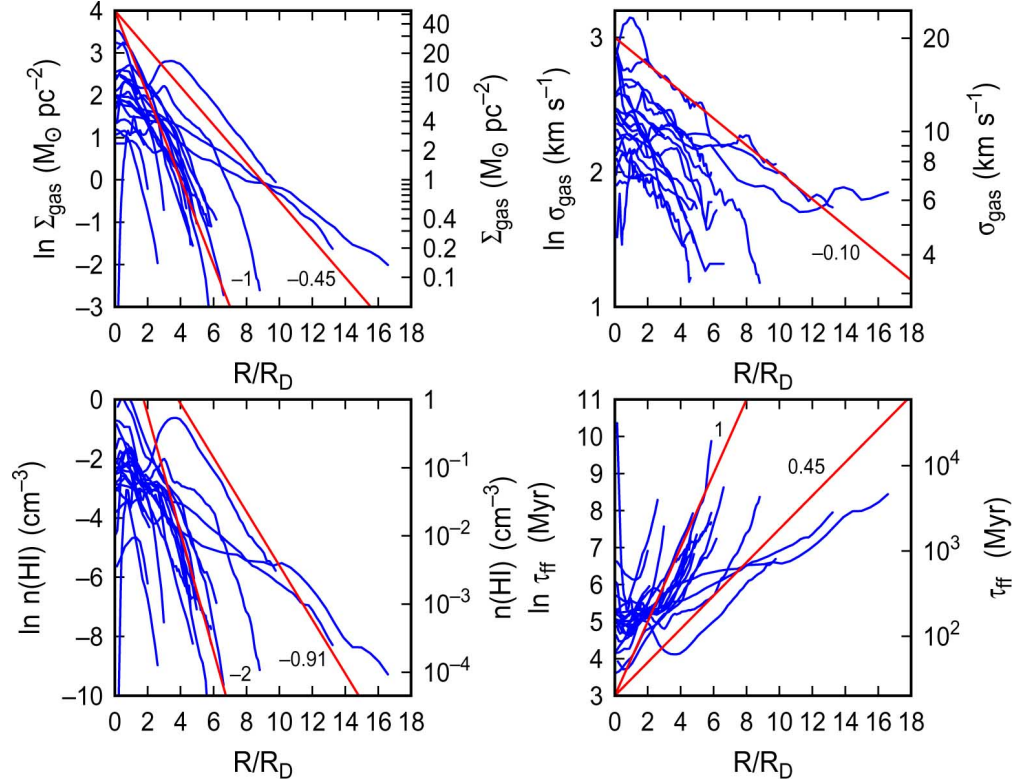


Fig. 11.— Radial profiles for quantities derived from the HI observations: surface density in the upper left, velocity dispersion in the upper right, 3D midplane density in the lower left and free fall time in the lower right. The plots are in log-linear space with the natural logarithms on the left-hand axes for comparison to the exponential disk profiles discussed elsewhere. The right-hand axes are plotted in physical units, again on a log scale. The slopes of the red lines are indicated. One red line in each panel has a slope given by a fit to the inner regions (Table 2) and another red line, if there is one, suggests a different slope for the gas in the outer region.